Adaptive Control for a Microgravity Vibration Isolation System

Final Report, 1 September 2004 to 31 March 2006

Research Supported by:
NASA Marshall Space Flight Center, Huntsville, AL
Grant No. NAG8-1292.

Principal Investigator: Dr. Anthony J. Calise*
Co-Principal Investigator: Dr. James I. Craig**
Research Engineer: Dr. Bong-Jun Yang+
Technical Advisor: Dr. Mark S. Whorton, NASA Marshall Space Flight Center

Georgia Institute of Technology
School of Aerospace Engineering
Atlanta, GA 30332-0150

* Professor, (404)894-7145, anthony.calise@ae.gatech.edu

** Professor, (404)894-3042, james.craig@ae.gatech.edu

+ Research Engineer II, (404)385-4940, jun.yang@ae.gatech.edu

Contents

Abstract

Most active vibration isolation systems that try to a provide quiescent acceleration environment for space-science experiments have utilized linear design methods. In this report, we address adaptive control augmentation of an existing classical controller that combines a high-gain acceleration inner-loop feedback together with a low-gain position outer-loop feedback to regulate the platform about its center position. The control design considers both parametric and dynamic uncertainties because the isolation system must accommodate a variety of payloads having different inertial and dynamic characteristics. We show how adaptive control is beneficial in three important aspects in design of a controller for uncertain systems: performance, robustness, and transient responses. First, performance is treated in the setting that an accelerometer and an actuator is located at the same location, as is the current hardware configuration for g-LIMIT. Second, robustness for the control system becomes more of an issue when the sensor is non-collocated with the actuator. We illustrate that adaptive control can stabilize otherwise unstable dynamics due to the presence of unmodelled dynamics. Third, transient responses of the position of the isolation system are significantly influenced by a high-gain acceleration controller when it includes integral action. An important aspect of the g-lIMIT is the accelerometer bias and the deviation of the platform it causes as a result of integral control. By employing adaptive neural networks for both the inner-loop and outer-loop controllers, we illustrate that adaptive control can improve both steady-state responses and transient responses in position. A feature in the design is that high-band pass and low pass filters are applied to the error signal used to adapt the weights in the neural network and the adaptive signals, so that the adaptive processes operate over targeted ranges of frequency. This prevents the inner and outer loop adaptive processes from interfering with each other.

Section 1

Introduction

The low-acceleration environment on the International Space Station (ISS) will enable microgravity science experiments that are practically impossible on the surface of the Earth. However, a variety of vibro-acoustic disturbances on the ISS are present and can degrade the performance of many microgravity experiments. In fact, the acceleration environment on the ISS is expected to exceed the requirements of many acceleration sensitive experiments[1] as shown in Figure 1.1(a). By comparing the requirement with the expected ISS acceleration in Figure 1.1(a), an isolation performance specification can be derived as in Figure 1.1(b). The isolation system must attenuate the ambient ISS acceleration by one order of magnitude at 0.1 Hz, which for a second order system implies maximum break-frequency of 0.01 Hz. That is, while the isolated system can transmit the quasi-steady accelerations of the vehicle below 0.01 Hz to the isolated assembly, it must attenuate all disturbances above 0.01 Hz. This performance specification requires the implementation of an active vibration isolation system because passive isolation systems, in general, are not able to provide sufficient attenuation of low vibration frequency disturbances.

An example of rack-level vibration isolation is the Active Rack Isolation System (ARIS)[2], the control architectures and flight-test results of which can be found in [3, 4]. In contrast to rack-level isolation systems, g-LIMIT (gLovebox Integrated Microgravity Isolation Technology) shown in Figure 1.2 is a microgravity vibration isolation system that is designed to isolate experiments at the payload level. The g-LIMIT hardware consists of the inertially isolated assembly to which an experiment is mounted and the base assembly that is rigidly attached to the Microgravity Science Glovebox (MSG) work volume floor. In order to provide a quiescent acceleration environment for an experiment, g-LIMIT utilizes six independent control actuation channels that apply six independent magnetic forces to a platform upon which the experiment resides. g-LIMIT is designed around three integrated isolator modules (IM's), each of which is comprised of a dual-axis magnetic actuator, two axes of acceleration sensing, and two axes of sensing the relative position of the isolated platform with respect to the base assembly[5]. Integrated into the base assembly and the isolated assembly is a snubber system which provides mechanical rattle-space constraints with a maximum relative displacement of 1.0 cm between the isolated assembly and the base assembly. The only mechanical connection between the isolated platform and the base assembly is the set of umbilicals that pass resources between the MSG and the experiment.

The design of an isolation system for g-LIMIT is a challenging problem due to the stringent performance requirement and static and dynamic uncertainties that arise due both to kinematic coupling between the platform and the mounted experiment as well as to the damping and stiffness properties of umbilicals. The mass and inertia properties of the system change considerably as various experiments utilize the isolation system during its operation. Unlike the rack-level isolation system where the rack structure is much more massive than the individual experiment, the mass and inertial variations in g-LIMIT are generally comparable to those of the isolation system and thus more problematic. The umbilicals are the primary load path for the ISS disturbances

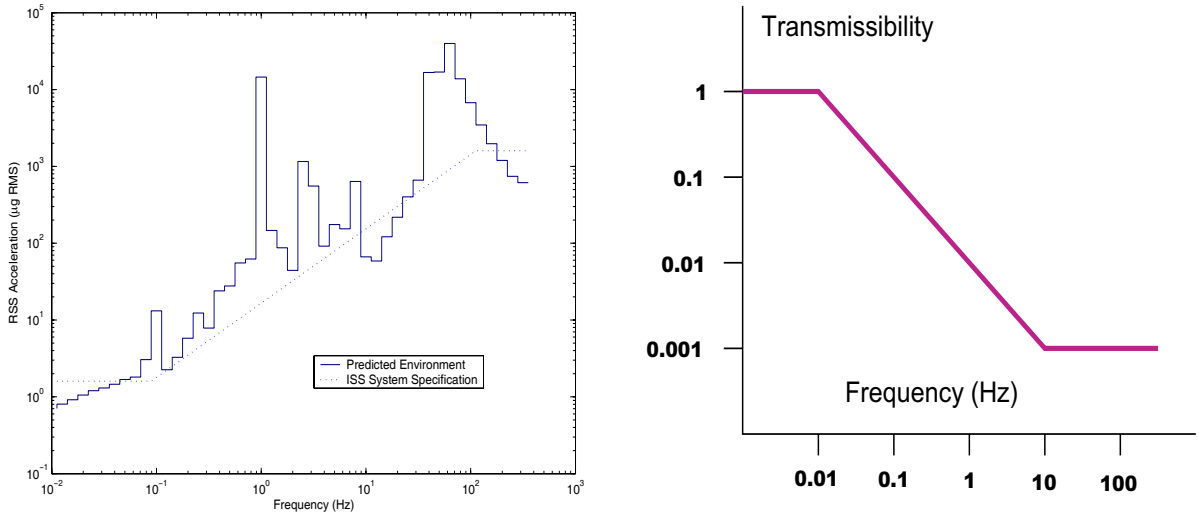

(a) Predicted RMS acceleration environment of the International Space Station

(b) Transmissibility Requirement

Figure 1.1: Frequency environment and requirement

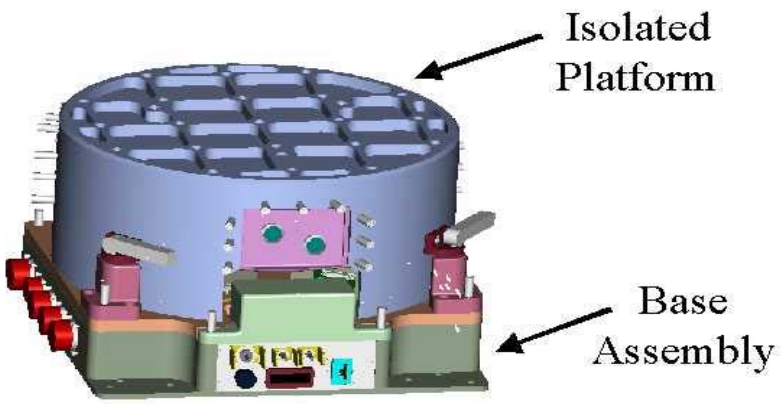

Figure 1.2: g-LIMIT System assembly

to the isolated system and the primary source of uncertainties for control system design since their stiffness and damping properties cannot be accurately measured on the ground due to gravitational deflections and coupling. Moreover, the flight-test results in [3] reveal the possibility of hysteresis in their stiffness properties. This may become a significant factor in a low-amplitude acceleration environment and may degrade the performance of the isolation system[3].

Most vibration isolation systems have used linear control methods[6, 7, 8, 9](an exception is found in [10]). For the design of a control system for g-LIMIT, a two-loop (inner/outer) architecture is employed. That is, a high-gain acceleration feedback is used to cancel the accelerations in the inner-loop, and a low-gain position feedback is added to the outer-loop to center the platform in the sway space and drive the platform to follow the quasi-steady motion of the vehicle. In [8], classical Proportional-Integral-Derivative (PID) controllers are designed for both the acceleration and position feedback. Fixed-order mixed H_2/μ control is considered for acceleration feedback in [9], the nominal performance and robustness of which are compared to those of a standard H_2 method.

In this report, we conceptually consider an adaptive control approach that augments the PID control design in

[8] to improve both nominal and robust performance. The adaptive elements are designed following the method described in [11, 12]. A neural network (NN) is employed to approximately cancel the uncertainty. It is well established that a NN can approximate any continuous function to any desired accuracy on a bounded set[13], and this has been one of the main reasons given for using a NN in control approaches[14, 15, 16]. In an output feedback setting, a method that uses a memory unit of input/output delays to approximate an uncertainty has been proposed[17, 18] and shown to be effective in output feedback applications[19, 20, 12, 21]. The method in [11] is selected for the design of adaptive control for g-LIMIT because with acceleration as the regulated output, the system is nonminimum phase, and therefore inversion-based feedback approaches[22, 23] cannot be applied.

The report is organized as follows. In Section 2 we present the problem of a controller design for g-LIMIT in a single-input single-output (SISO) setting. The dynamics are represented by a single mass-spring-damper system on which an experiment, modelled as two mass-spring-damper system, is mounted. Depending on where the accelerometer is mounted, the actuator/sensor are either collocated or non-collocated. The architecture for an existing control system for g-LIMIT in [8] is also introduced.

In Section 3 we consider the case where the accelerometer and the actuators are collocated. The collocated set-up for a control system design has some inherent robustness over certain parametric and dynamic uncertainties[24], and the existing control system maintains its stability. When the performance specification is given only in terms of steady-state responses of the acceleration, we show that adaptive control significantly enhances its isolation performance over the frequency range of interest.

In Section 4 we consider a case of non-collocated configuration for the accelerometer and the actuator. To study this case we redesigned the so-called existing control system to account for the non-collocation. However, the new design does encounter a stability problem in the presence of parametric uncertainty. By employing a NN, we show that the stability of the nominal controlled system is recovered

In Section 5 we consider augmenting both the inner-loop and outer-loop controllers by two NNs and show that improvement both in isolation performance and in transient responses is feasible when the design bandwidths are not overlapping.

Section 2

System Dynamics and Existing Control System

For simplicity motion along a single axis of a g-LIMIT platform on which a flexible experiment is mounted is depicted in Figure 2.1. The mass M_1 represents the isolated platform with a nominal experiment mass, M_2 is the uncertainty in the mass of the experiment that is mounted on the platform, and M_3 and M_4 represent flexibility in the experiment. The term x_o represents the displacement of the base, x_1 is the relative displacement from the

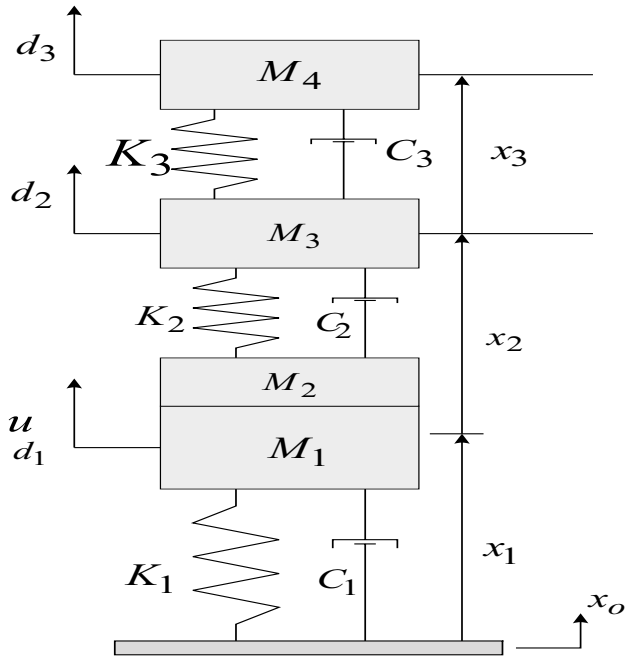

Figure 2.1: Mass spring damper with unmodeled dynamics

base, x_2 is the relative displacement between M_2 and M_3, and x_4 is the relative displacement between M_3 and M_4, respectively. The equations of motion for the system in Figure 2.1 are:

$$\begin{aligned} &M_c(\ddot{x}_o + \ddot{x}_1) + C_1\dot{x}_1 + K_1x_1 - C_2\dot{x}_2 - K_2x_2 = u + d_1, \\ &M_3(\ddot{x}_o + \ddot{x}_1 + \ddot{x}_2) + C_2\dot{x}_2 + K_2x_2 - C_3\dot{x}_3 - K_3x_3 = d_2, \\ &M_4(\ddot{x}_o + \ddot{x}_1 + \ddot{x}_2 + \ddot{x}_3) + C_3\dot{x}_3 + K_3x_3 = d_3 \end{aligned} \tag{2.1}$$

where $M_c = M_1 + M_2$, and d_1, d_2, d_3 represent external disturbances applied to M_1, M_3, M_4, respectively.

When the acceleration sensor is located at M_1, the sensor is collocated with the actuator, and two measured outputs (the *absolute* acceleration of M_1 and the *relative* displacement x_1) are:

$$y_1 = \ddot{x}_o + \ddot{x}_1,\ y_2 = x_1. \tag{2.2}$$

This actuator and sensor configuration represents the case in which the acceleration is measured at the platform level of g-LIMIT. On the other hand, when the acceleration at the experiment for space science is measured, the accelerometer is assumed to be mounted at the location of M_3 and constitutes a non-collocated problem. That is, the two measured outputs are expressed by

$$y_1 = \ddot{x}_o + \ddot{x}_1 + \ddot{x}_2,\ y_2 = x_1. \tag{2.3}$$

Defining $\boldsymbol{x} = [x_1\ \dot{x}_1,\ x_2,\ \dot{x}_2, x_3, \dot{x}_3]^T$, we can write the dynamics in a state space form:

$$\begin{aligned} \dot{\boldsymbol{x}} &= A\boldsymbol{x} + \boldsymbol{b}u + \boldsymbol{b}_f\ddot{x}_o + B_d\boldsymbol{d}, \quad \boldsymbol{x} \in \mathbb{R}^{6\times 1} \\ y_1 &= \boldsymbol{c}_1^T\boldsymbol{x} + D_u u + D_d\boldsymbol{d}, \\ y_2 &= \boldsymbol{c}_2^T\boldsymbol{x}, \end{aligned} \tag{2.4}$$

where $\boldsymbol{d} = [d_1,\ d_2,\ d_3]^T$, where $\boldsymbol{c}_1$, D_u, D_d depend on the location of the accelerometer, and $\boldsymbol{c}_2 = [1, 0_{1\times 5}]^T$.

The objective of the vibration isolation system is to design a control law for u so as to cancel the acceleration, y_1, by an acceleration feedback while centering M_1 (*i.e.*, regulating y_2) using position feedback. The position must be restricted within a limit of 1.0 m. The performance of the isolation system will be measured with the control law applied to the system in (2.4). For the existing controller, a high-gain, high-bandwidth acceleration feedback inner-loop controller was designed to satisfy the vibration suppression requirement, and a low-gain, low-bandwidth position feedback outer-loop controller was designed to regulate position about the center in the sway space. That is, a single control is used both to suppress the acceleration and to regulate the position, and, in order to reduce the spill-over effects from one controller to the other, these controllers are designed so that the bands of frequency over which they have significant loop gain are separated. The existing control system described in [8] is shown in Figure 2.2. The commanded relative position (generally zero) is x_c, and n represents the accelerometer error (due to sensor bias).

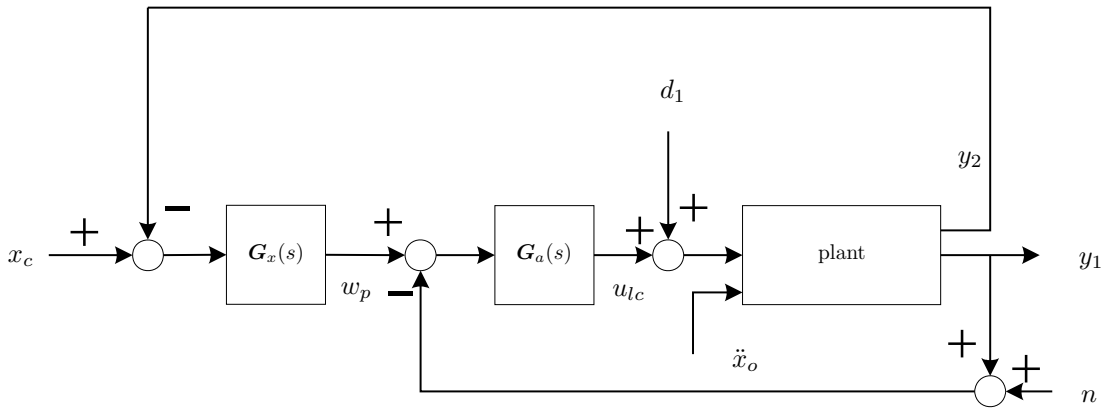

Figure 2.2: Existing control system architecture

Section 3

Inner-Loop Adaptive Control for the Collocated Control Problem

3.1 Analysis of the Existing Control system

When the accelerometer is located at M_1, the two measured outputs are given in (2.2), and the matrices $\boldsymbol{c}_1$, D, and D_d in (2.4) are as follows

$$\boldsymbol{c}_1^T = \begin{bmatrix} -\frac{K_1}{M_c} & -\frac{C_1}{M_c} & \frac{K_2}{M_c} & \frac{C_2}{M_c} & 0 & 0 \end{bmatrix},\ D_u = \frac{1}{M_c},\ D_d = \begin{bmatrix} \frac{1}{M_c} & 0 & 0 \end{bmatrix}. \tag{3.1}$$

The parameter values are: $M_1 = 17.8488$, $C_1 = 0.5242$, $K_1 = 6.1574$, $M_2 = 5$, $M_3 = 5$, $M_4 = 5$, $C_2 = 1 \times 10^{-17}$, $C_3 = 1 \times 10^{-17}$, $K_2 = 15$, and $K_3 = 25$.

The plant model, which is used in the design of the feedback control system, consists of a single mass-spring-damper

$$\hat{M}(\ddot{x}_o + \ddot{x}) + \hat{C}\dot{x} + \hat{K}x = u, \tag{3.2}$$

where $\hat{M} = 17.8488$, $\hat{C} = 0.5242$, and $\hat{K} = 6.1574$. This plant model implies that M_3 and M_4 represent unmodelled dynamics. With the outputs corresponding to those in (2.2) and by letting $\boldsymbol{x}_m = [x,\ \dot{x}]^T$, the plant model in (3.2) can also be expressed in a state-space form:

$$\begin{aligned} \dot{\boldsymbol{x}}_m &= A_m \boldsymbol{x}_m + \boldsymbol{b}_m(u + d_1) + \boldsymbol{b}_{m_f}\ddot{x}_o, \quad \boldsymbol{x}_m \in \mathbb{R}^{2\times 1} \\ y_{m_1} &= \boldsymbol{c}_{m_1}^T \boldsymbol{x}_m + D_m u, \\ y_{m_2} &= \boldsymbol{c}_{m_2}^T \boldsymbol{x}_m. \end{aligned} \tag{3.3}$$

Figure 3.1 compares the frequency response of the plant model with that of the system in (2.4). The disturbance attenuation requirement in Figure 1.1(b) is associated with the *transmissibility*, $\frac{\ddot{x}}{\ddot{x}_o} = G_{b2a}(s)$, from the base to the isolated assembly (M_1) and shown in Figure 3.1(c). The control system design generally involves $G_{u2a} = \frac{y_1(s)}{u(s)}$ and $G_{u2x} = \frac{y_2(s)}{u(s)}$ which are shown in Figures 3.1(a) and 3.1(b). Note that the transfer functions from the input, u, to the acceleration and the position are the same as those from the disturbance, d_1, to the acceleration and the position since u and d_1 represent forces that are applied as the same location.

In the collocated case, the existing controller, $G_a(s)$ in Figure 2.2, consists of a PI controller

$$u_{lc} = G_a(s)\big[w_p - (y_1 + n)\big] = \frac{K_{I_i} + K_{I_p}s}{s}[w_p - (y_1 + n)], \tag{3.4}$$

where $K_{I_i} = 250$, and $K_{I_p} = 0.4175$. In a state space form, it is given by

$$\begin{aligned} \dot{\eta}_i &= w_p - (y_1 + n), \\ u_{lc} &= K_{I_i}\eta_i + K_{I_p}(w_p - (y_1 + n)). \end{aligned} \tag{3.5}$$

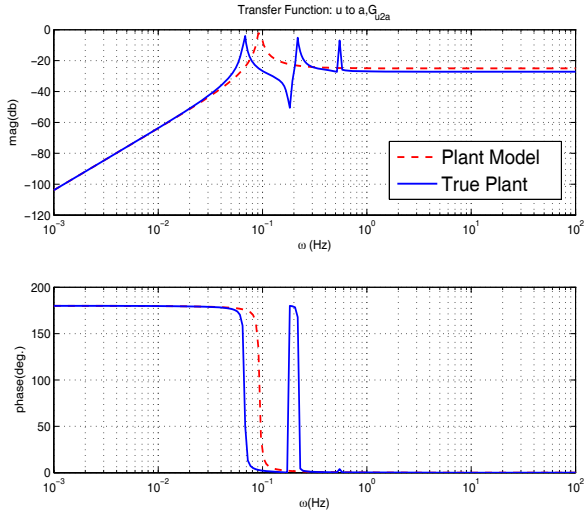

(a) Bode plot for G_{u2a} ($= \frac{y_1(s)}{u(s)}$).

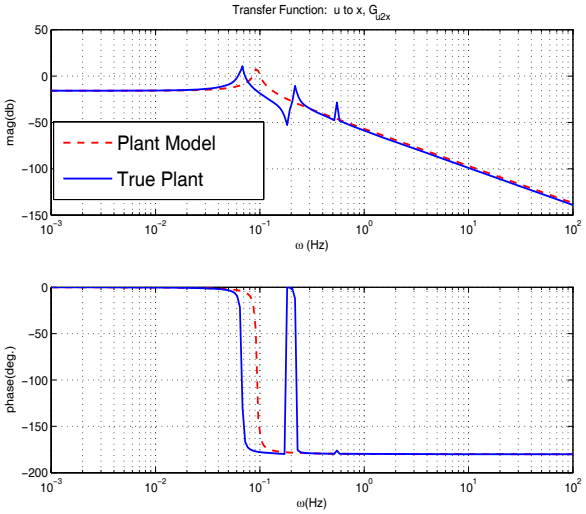

(b) Bode plot for G_{u2x} ($= \frac{y_2(s)}{u(s)}$).

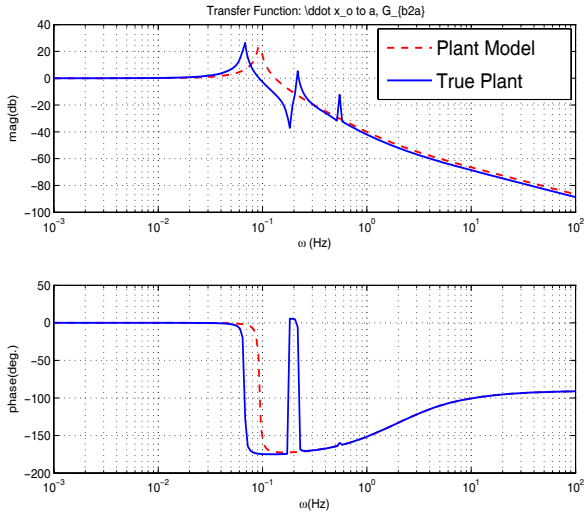

(c) Bode plot for G_{b2a} ($= \frac{y_1(s)}{\ddot{x}_o(s)}$).

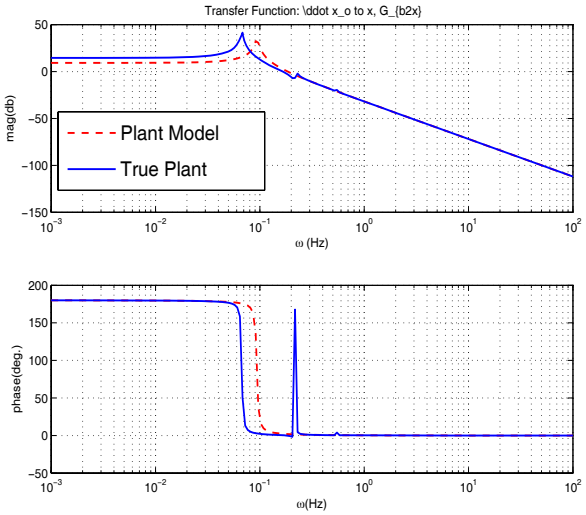

(d) Bode plot for G_{b2x} ($= \frac{y_2(s)}{\ddot{x}_o(s)}$).

Figure 3.1: Frequency response of various transfer functions

Applying the controller in (3.4) to both the plant model in (3.3) and the true plant in (2.4) leads to the frequency responses shown in Figure 3.2. The overall system frequency response reveals that the mounted experiment does not have much influence on the isolation system. As a matter of fact, the root locus diagrams in Figures 3.3 and 3.4 reveal that both the plant model (Figures 3.3) and the true plant (Figure 3.4) are stable under the regulation of the acceleration controller in (3.4), and have a theoretically infinite gain margin. Figure 3.2(c) shows that the acceleration controller is properly designed to meet the specified transmissibility. The frequency response from the sensor error to the relative position as shown in Figure 3.2(f) reveals an undesirable effect due to the accelerometer, which suggests that without compensation the accelerometer bias can cause a large position deviation from the center of the sway space.

The outer-loop controller, $G_x(s)$ in Figure 2.2, is designed as a PID controller in which integral action is required to remove the effect of the accelerometer bias. Since direct implementation of derivative control amplifies the sensor noise and causes numerical problems, the PID controller is realized as

$$w_p(s) = [K_p + K_d \frac{s}{\frac{1}{50}s + 1} + \frac{K_i}{s}](x_c - y_2), \tag{3.6}$$

where $K_i = 3 \times 10^{-6}$, $K_d = 0.02063$, and $K_p = 0.00054$. In a state space form, it is given by

$$\begin{aligned} \dot{\boldsymbol{\eta}}_o &= A_c \boldsymbol{\eta}_o + \boldsymbol{b}_c (x_c - y_2) \\ w_p &= \boldsymbol{c}_c^T \boldsymbol{\eta}_o + D_c (x_c - y_2). \end{aligned} \tag{3.7}$$

Figure 3.5 shows the frequency response of the overall closed-loop system. On the whole, the effect of unmodelled dynamics is negligible, implying that the existing design is robust for the present collocated set-up. Figure 3.5(a) indicates that the existing control system meets the performance requirement for vibration isolation. That is, if the base excitations are the only source of external disturbances, the performance of the isolation system is acceptable. Figure 3.5(f) indicates that the outer-loop position controller removes the effect of accelerometer bias in steady state.

3.2 Inner-Loop Control Augmentation

We augment the inner-loop acceleration controller using the method in [11], which is depicted in Figure 3.6. The goal is to improve the level of vibration suppression that cannot otherwise be achieved through linear control design. However, an immediate issue is that, with acceleration as the regulated output, the relative degree of the design is 0, whereas the approach in [11] assumes that the relative degree is greater than 0. To circumvent this problem, we introduce an integrator before the control input so that the system has relative degree 1 ("dynamic extension" [25]) in order to augment the existing controller with an adaptive element. With dynamic extension, $\dot{\eta} = v,\ u = \eta$, the system in (2.4) is rewritten as

$$\begin{aligned} \dot{\boldsymbol{x}}_a &= \boldsymbol{A}_a \boldsymbol{x}_a + \boldsymbol{b}_a v + \boldsymbol{b}_{a_f} \ddot{x}_o + B_{a_d} \boldsymbol{d} \\ y_1 &= \boldsymbol{c}_{a_1}^T \boldsymbol{x}_a + D_d \boldsymbol{d} \\ y_2 &= \boldsymbol{c}_{a_2}^T \boldsymbol{x}_a \end{aligned} \tag{3.8}$$

where

$$\begin{aligned} &\boldsymbol{x}_a = \begin{bmatrix} \boldsymbol{x} \\ \eta \end{bmatrix},\ A_a = \begin{bmatrix} A & \boldsymbol{b} \\ 0 & 0 \end{bmatrix},\ \boldsymbol{b}_a = \begin{bmatrix} 0 \\ 1 \end{bmatrix},\ \boldsymbol{b}_{a_f} = \begin{bmatrix} \boldsymbol{b}_f \\ 0 \end{bmatrix},\ B_{a_d} = \begin{bmatrix} B_d \\ 0 \end{bmatrix} \\ &\boldsymbol{c}_{a_1} = \begin{bmatrix} \boldsymbol{c}_1^T & D_u \end{bmatrix}^T,\ \boldsymbol{c}_{a_2} = \begin{bmatrix} \boldsymbol{c}_2^T & 0 \end{bmatrix}^T. \end{aligned} \tag{3.9}$$

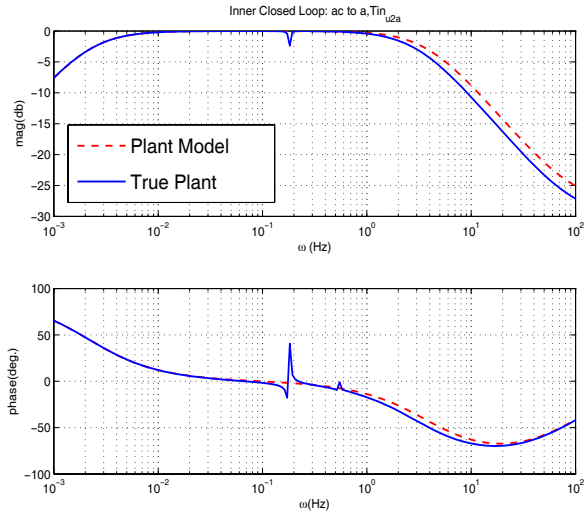

(a) Bode plot for $\frac{y_1}{w_p}$.

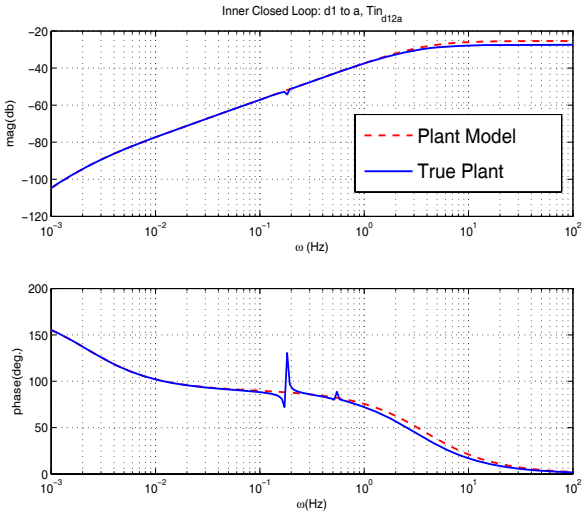

(b) Bode plot for $\frac{y_1}{d_1}$.

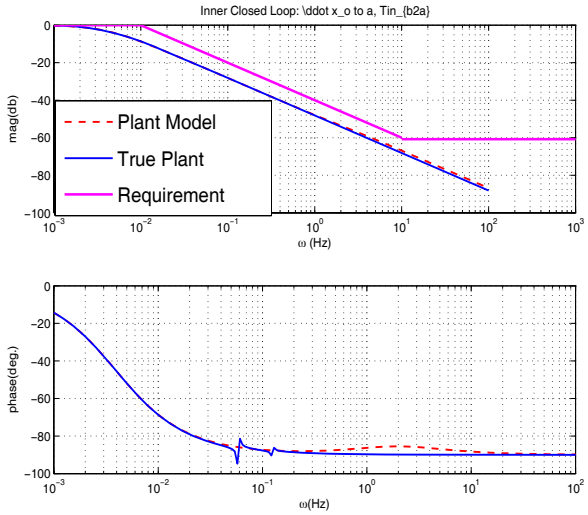

(c) Bode plot for $\frac{y_1}{\ddot{x}_o}$.

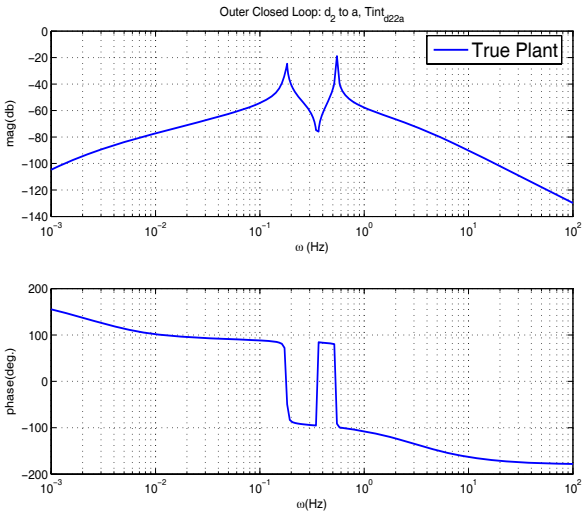

(d) Bode plot for $\frac{y_1}{d_2}$.

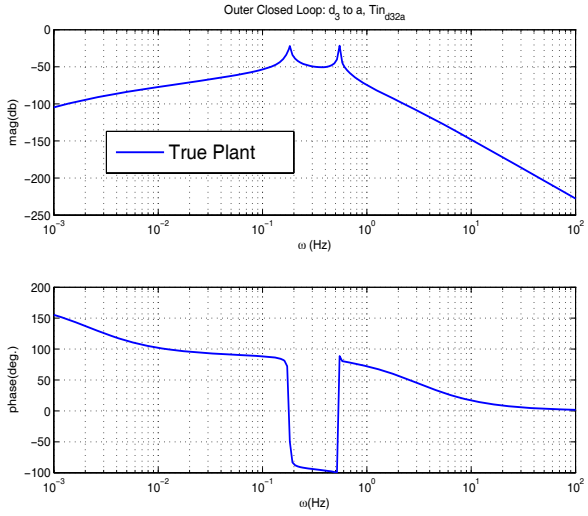

(e) Bode Plot for $\frac{y_1}{d_3}$.

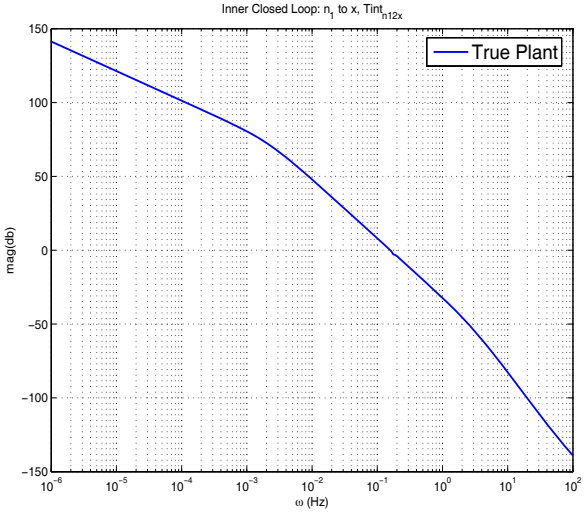

(f) Bode plot for $\frac{y_2}{n}$.

Figure 3.2: Frequency responses for inner-loop transfer functions

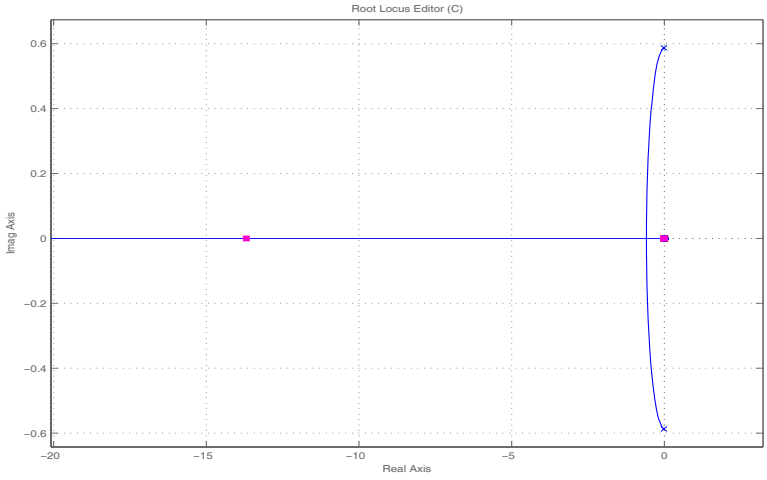

Figure 3.3: Root locus for the inner-loop of the plant model

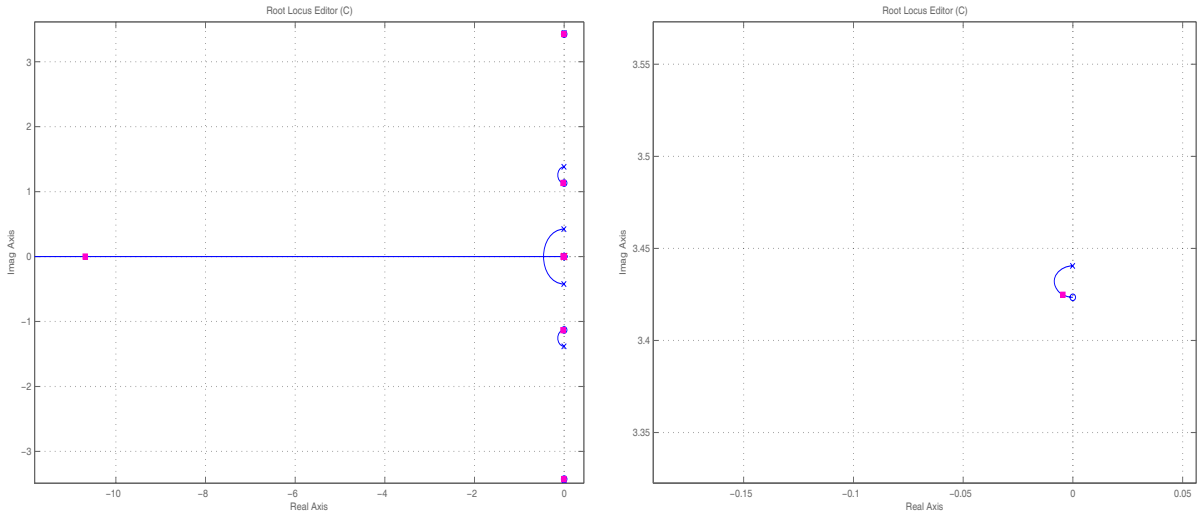

(a) Root locus for the true plant

(b) Zoomed plot for the third flexible mode

Figure 3.4: Root locus for the inner-loop of the true plant

In the same manner, with $\ddot{x}_o = d_1 = 0$, the extended plant model corresponding to (3.8) is described by

$$\begin{aligned} \dot{\boldsymbol{x}}_{a_m} &= A_{a_m}\boldsymbol{x}_{a_m} + \boldsymbol{b}_{a_m} v, \\ y_{m_1} &= \boldsymbol{c}_{a_{m_1}}^T \boldsymbol{x}_{a_m}, \\ y_{m_2} &= \boldsymbol{c}_{a_{m_2}}^T \boldsymbol{x}_{a_m}, \end{aligned} \tag{3.10}$$

where

$$\begin{aligned} &\boldsymbol{x}_{a_m} = \begin{bmatrix} \boldsymbol{x}_m \\ \eta \end{bmatrix}, \; A_{a_m} = \begin{bmatrix} A_m & \boldsymbol{b}_m \\ 0 & 0 \end{bmatrix}, \; \boldsymbol{b}_{a_m} = \begin{bmatrix} 0 \\ 1 \end{bmatrix}, \\ &\boldsymbol{c}_{a_{m_1}} = \begin{bmatrix} \boldsymbol{c}_{m_1} & D_m \end{bmatrix}^T, \; \boldsymbol{c}_{a_{m_2}} = \begin{bmatrix} \boldsymbol{c}_{m_2} & 0 \end{bmatrix}^T. \end{aligned} \tag{3.11}$$

3.2.1 Inner-Loop Reference Model

The inner-loop reference model in Figure 3.6 consists of the plant model in (3.3) regulated by the PI controller in (3.4) with $\ddot{x}_o = d_1 = n = 0$. The inner-loop reference model can also be viewed as the closed-loop system of

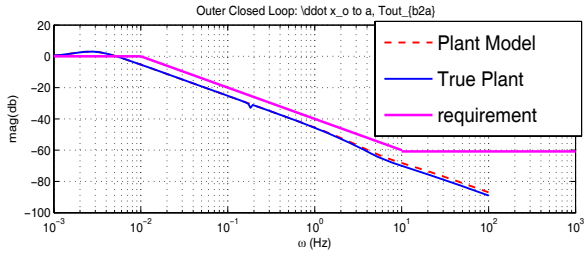

(a) Bode plot for $\frac{y_1}{\ddot{x}_o}$.

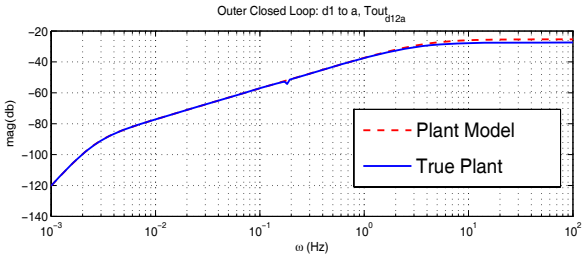

(b) Bode plot for $\frac{y_1}{d_1}$.

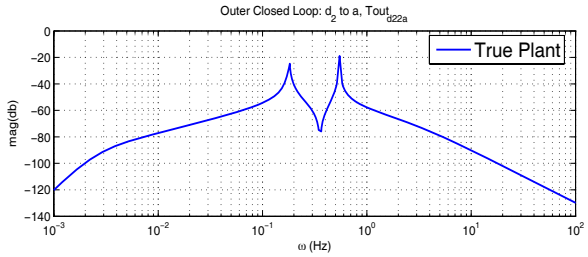

(c) Bode plot for $\frac{y_1}{d_2}$.

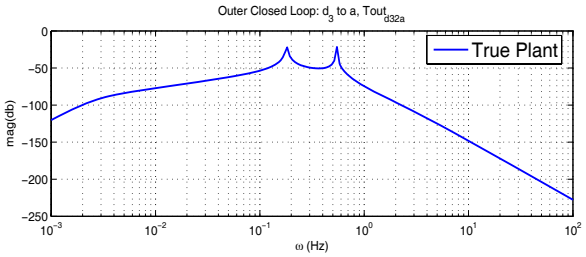

(d) Bode plot for $\frac{y_1}{d_3}$.

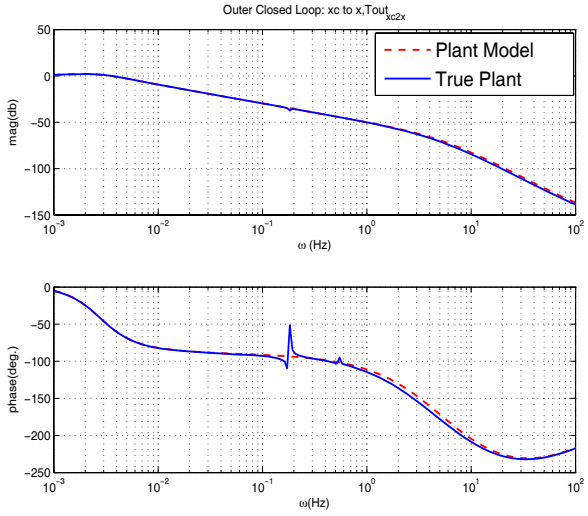

(e) Bode plot for $\frac{y_2}{x_c}$.

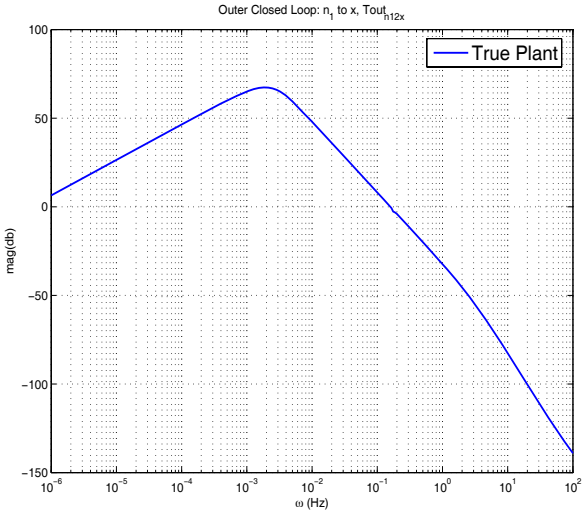

(f) Bode plot for $\frac{y_2}{n}$.

Figure 3.5: Frequency responses for overall (inner-loop+outer-loop) transfer functions

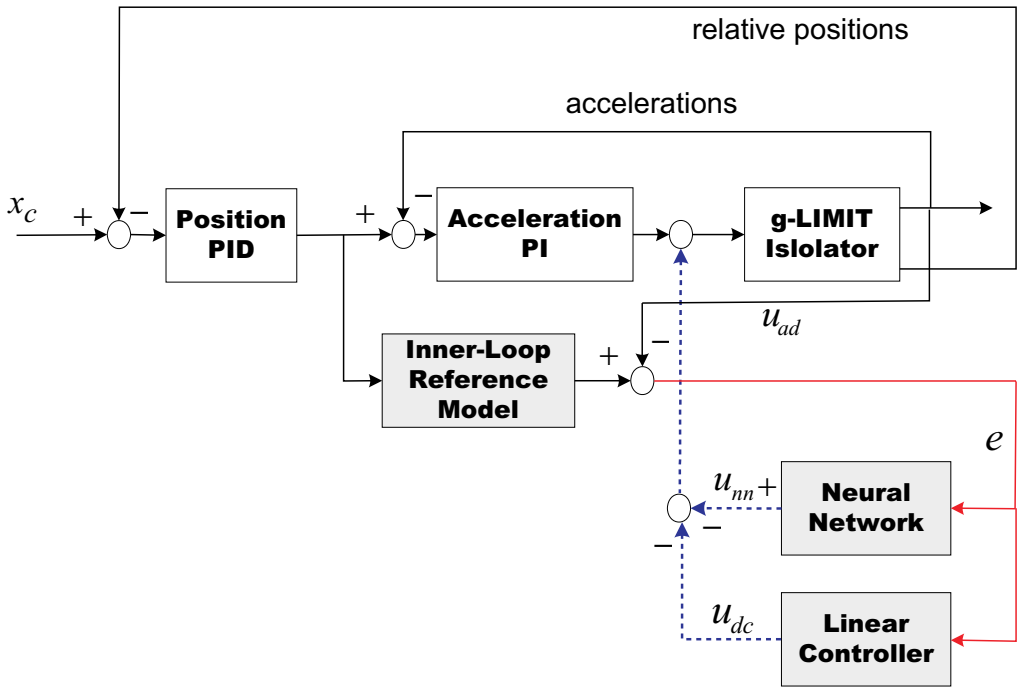

Figure 3.6: Closed Inner-Loop Reference Model based Augmentation Architecture

the extended plant model in (3.10) and the PD controller as shown in Figure 3.7.

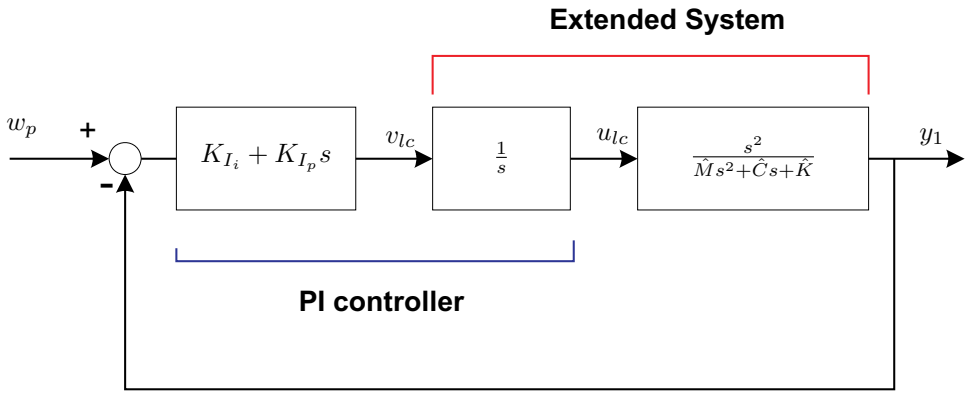

Figure 3.7: Inner-Loop Reference Model

To apply the method in [11], the system in (3.10) is transformed into a normal form[25]

$$\begin{aligned} \dot{y}_{m_1} =& a_1 y_{m_1} + \boldsymbol{h}_o^T \boldsymbol{z}_m + D_m v \\ \dot{\boldsymbol{z}}_m =& \boldsymbol{g}_o y_{m_1} + F_o \boldsymbol{z}_m, \end{aligned} \tag{3.12}$$

where $\boldsymbol{z}_m = [x_{m_1}\ x_{m_2}]^T$. The signal, $v_{lc}(= \dot{u}_{cl})$, is obtained by solving the following algebraic loop

$$\begin{aligned} v_{lc} =& K_{I_i}(w_p - y_{m_1}) + K_{I_p}(\dot{w}_p - \dot{y}_{m_1}) \\ =& K_{I_i}(w_p - \boldsymbol{c}_{a_{m_1}}^T \boldsymbol{x}_{a_m}) + K_{I_p}(\dot{w}_p - \boldsymbol{c}_{a_{m_1}}^T A_{a_m} \boldsymbol{x}_{a_m} - \boldsymbol{c}_{a_{m_1}}^T \boldsymbol{b}_{a_m} v_{lc}). \end{aligned} \tag{3.13}$$

This leads to

$$v_{lc} = -\frac{1}{1+K_{I_p}D_m}\left[K_{I_i}+K_{I_p}a_1\right]y_{m_1} - \frac{K_{I_p}}{1+K_{I_p}D_m}\boldsymbol{h}_o^T\boldsymbol{z}_m + \frac{1}{1+K_{I_p}D_m}\left[K_{I_i}w_p + K_{I_p}\dot{w}_p\right]. \tag{3.14}$$

Applying the control signal, v_{lc}, in (3.14) to the normal-form extended plant model in (3.12) leads to the following inner-loop reference model

$$\dot{\boldsymbol{\zeta}}_m = \bar{A}\boldsymbol{\zeta}_m + \bar{\boldsymbol{b}}_p\begin{bmatrix} w_p \\ \dot{w}_p \end{bmatrix}, \tag{3.15}$$

where $\boldsymbol{\zeta}_m = [y_{m_1}\ \boldsymbol{z}_m^T]^T$, and

$$\bar{A} = \begin{bmatrix} a_1 - \frac{D_m(K_{I_i}+K_{I_p}a_1)}{1+K_{I_p}D_m} & 1-\frac{K_{I_p}}{1+K_{I_p}D_m} \\ \boldsymbol{g}_o & F_o \end{bmatrix},\ \bar{\boldsymbol{b}}_p = \begin{bmatrix} \frac{K_{I_i}}{1+K_{I_p}D_m} & \frac{K_{I_p}}{1+K_{I_p}D_m} \\ 0 & 0 \end{bmatrix}. \tag{3.16}$$

3.2.2 Error Dynamics

Compared to the extended plant model in (3.12), the extend system in (3.8) can be written in normal form

$$\begin{aligned} \dot{y}_1 =& a_1y_1 + \boldsymbol{h}_o^T\boldsymbol{z}_1 + D_m(v+\Delta_1) \\ \dot{\boldsymbol{z}}_1 =& \boldsymbol{g}_o y_1 + F_o\boldsymbol{z}_1 + \boldsymbol{\Delta}_2(y_1,\boldsymbol{z}_1,\boldsymbol{z}_2) \\ \dot{\boldsymbol{z}}_2 =& F_2\boldsymbol{z}_2 + F_1\boldsymbol{z}_1 + \boldsymbol{g}_1y_1. \end{aligned} \tag{3.17}$$

where $\boldsymbol{z}_1$ represents states corresponding to $\boldsymbol{z}_m$ in (3.12), and $\boldsymbol{z}_2$ results from the stable unmodelled dynamics. The unmatched uncertainty, $\boldsymbol{\Delta}_2 = \dot{\boldsymbol{z}}_1 - \boldsymbol{g}_o y_1 - F_o\boldsymbol{z}_1$, is assumed to satisfy the linear growth assumption that is required for the stability proof [11]. The matched uncertainty that will be compensated for by the adaptive elements is defined by

$$\Delta_1(y_1,\boldsymbol{z}_1,\boldsymbol{z}_2,v) = \frac{1}{D_m}[\boldsymbol{c}_{a_1}^TA_a\boldsymbol{x}_a + \boldsymbol{c}_{a_1}^T\boldsymbol{b}_av + \boldsymbol{c}_{a_1}^T\boldsymbol{b}_{a_f}\ddot{x}_o + \boldsymbol{c}_{a_1}^TB_{a_d}\boldsymbol{d} + D_d\dot{\boldsymbol{d}} - [a_1y_1 + \boldsymbol{h}_o^T\boldsymbol{z}_1 + D_mv]]. \tag{3.18}$$

Let

$$v = v_{lc} + v_{ad}. \tag{3.19}$$

The signal, v_{lc} ($=\dot{u}_{lc}$), is the PD control signal for the extended system in (3.17)), and it can be derived in the same manner as the inner-loop reference model is derived:

$$\begin{aligned} v_{lc} =& -\frac{1}{1+K_{I_p}D_m}\left[K_{I_i}+K_{I_p}a_1\right]y_1 - \frac{K_{I_p}}{1+K_{I_p}D_m}\boldsymbol{h}_o^T\boldsymbol{z}_1 + \frac{1}{1+K_{I_p}D_m}\left[K_{I_i}w_p + K_{I_p}\dot{w}_p\right] + \\ & \frac{K_{I_p}D_m}{1+K_{I_p}D_m}[-v_{ad} - \Delta_1(y_1,\boldsymbol{z}_1,\boldsymbol{z}_2,v)]. \end{aligned} \tag{3.20}$$

Applying v_{lc} in (3.20) to the system in (3.17) results in the following closed-loop system

$$\begin{aligned} \dot{\boldsymbol{\zeta}} =& \bar{A}\boldsymbol{\zeta} + \bar{\boldsymbol{b}}_p\begin{bmatrix} w_p \\ \dot{w}_p \end{bmatrix} + \bar{\boldsymbol{b}}(v_{ad}+\Delta_1) + \bar{B}_\Delta\boldsymbol{\Delta}_2 \\ \dot{\boldsymbol{z}}_2 =& F_2\boldsymbol{z}_2 + F_1\boldsymbol{z}_1 + \boldsymbol{g}_1y_1, \end{aligned} \tag{3.21}$$

where

$$\bar{\boldsymbol{b}} = \begin{bmatrix} (1-\frac{K_{I_p}}{1+K_{I_p}D_m})D_m \\ 0 \end{bmatrix},\ \bar{B}_\Delta = \begin{bmatrix} 0_{1\times2} \\ I_{2\times2} \\ 0_{4\times2} \end{bmatrix}. \tag{3.22}$$

By defining the error vector as

$$\boldsymbol{E} = \boldsymbol{\zeta}_m - \boldsymbol{\zeta}, \tag{3.23}$$

we can derive the following error dynamics

$$\begin{aligned}\dot{\boldsymbol{E}} =&\bar{A}\boldsymbol{E} - \bar{\boldsymbol{b}}(v_{ad} + \Delta_1) - \bar{B}_\Delta \boldsymbol{\Delta}_2 \\ \dot{\boldsymbol{z}}_2 =&F_2\boldsymbol{z}_2 + F_1\boldsymbol{z}_1 + \boldsymbol{g}_1 y_1 \\ e_1 =&y_{m_1} - y_1 = \bar{\boldsymbol{c}}^T\boldsymbol{E}\end{aligned} \tag{3.24}$$

where $\bar{\boldsymbol{c}} = \begin{bmatrix} 1 & 0_{1\times 2} \end{bmatrix}^T$.

3.2.3 Linear Controller

The eigenvalues of the matrix, $\bar{A}$, are located at -13.6905, -0.0246, and 0. The pole located at the origin results from the integrator in the PI controller. Since the approach in [11] requires $\bar{A}$ to be Hurwitz, we add an additional controller to stabilize the error dynamics in (5.20). Let

$$v_{ad} = -v_{dc} - v_{nn}, \tag{3.25}$$

where the additional linear controller is designed as a linear quadratic Gaussian compensator

$$\begin{aligned}\dot{\boldsymbol{x}}_{dc} &= A_{dc}\boldsymbol{x}_{dc} + \boldsymbol{b}_{dc}e_1 \\ v_{dc} &= \boldsymbol{c}_{dc}^T\boldsymbol{x}_{dc} + d_{dc}e_1.\end{aligned} \tag{3.26}$$

Combining the compensator in (3.26) with the error dynamics in (5.20) leads to the closed-loop error dynamics

$$\dot{\boldsymbol{E}}_a = \bar{A}_a\boldsymbol{E}_a + \bar{\boldsymbol{b}}_a(v_{nn} - \Delta_1) - \bar{B}_{a_\Delta}\boldsymbol{\Delta}_2, \tag{3.27}$$

where

$$\bar{A}_a = \begin{bmatrix} \bar{A} + \bar{\boldsymbol{b}}d_{dc}\bar{\boldsymbol{c}}^T & \bar{\boldsymbol{b}}\boldsymbol{c}_{dc}^T \\ d_{dc}\bar{\boldsymbol{c}}^T & A_{dc} \end{bmatrix},\ \bar{\boldsymbol{b}}_a = \begin{bmatrix} \bar{\boldsymbol{b}} \\ 0 \end{bmatrix},\ \bar{B}_{a_\Delta} = \begin{bmatrix} \bar{B}_\Delta \\ 0 \end{bmatrix}. \tag{3.28}$$

The eigenvalues of $\bar{A}_a$ are $-13.6905, -13.6897, -2.35, -0.3332, -0.0069$, and -0.0006. Since $\bar{A}_a$ is Hurwitz, for any $Q_a > 0$, there exists a $P_a > 0$ such that

$$\bar{A}_a P_a + P_a\bar{A}_a + Q_a = 0. \tag{3.29}$$

3.3 The Adaptive Element

A single hidden-layer NN is used to approximate an unknown function. The result in [18] establishes a universal approximation for an unknown function $\Delta(x, u)$ of states in a bounded, observable process using a memory unit of sampled input/output pairs. For arbitrary $\epsilon^* > 0$, there exist bounded constant weights, $\boldsymbol{M}, N$, such that:

$$\Delta = \boldsymbol{M}^T\boldsymbol{\sigma}(N^T\boldsymbol{\eta}) + \varepsilon(\boldsymbol{\mu}),\ \ \|\varepsilon(\boldsymbol{\mu})\| \leq \epsilon^*, \tag{3.30}$$

where $\varepsilon(\boldsymbol{\mu})$ is the NN reconstruction error and $\boldsymbol{\mu}$ is the network input vector

$$\begin{aligned}\boldsymbol{\mu}(t) &= \begin{bmatrix} 1 & \bar{\boldsymbol{u}}_d^T(t) & \bar{\boldsymbol{y}}_d^T(t) \end{bmatrix}^T \\ \bar{\boldsymbol{u}}_d^T(t) &= [u(t) \quad u(t-d) \quad \cdots u(t-(n_1-r-1)d)]^T \\ \bar{\boldsymbol{y}}_d^T(t) &= [y(t) \quad y(t-d)\cdots y(t-(n_1-1)d)]^T\end{aligned} \tag{3.31}$$

in which n_1 is the length of the window and is generally required to be greater than or equal to the system dimension, $d > 0$ is a time-delay, r is the relative degree of the output, $\boldsymbol{\sigma}$ is a vector of squashing functions, $\sigma(\cdot)$, whose i^{th} element is defined as $\left[\boldsymbol{\sigma}(N^T\boldsymbol{\mu})\right]_i = \sigma\left[(N^T\boldsymbol{\mu})_i\right]$. The squashing functions are chosen as sigmoidal functions

$$[\boldsymbol{\sigma}(N^T\boldsymbol{\mu})]_i = \frac{1}{1 + e^{-a(N^T\boldsymbol{\mu})_i}},\ i = 1, \ldots, n_\sigma. \tag{3.32}$$

where $a = 1$ represents the activation potential, and n_σ is the number of neurons in the hidden layer.

3.4 Adaptive Control Design

A single hidden layer NN is introduced to approximate Δ_1 in (3.18), and the adaptive signal, v_{nn}, is designed as

$$v_{nn} = \widehat{\boldsymbol{M}}_a^T \boldsymbol{\sigma}(\widehat{N}_a^T \boldsymbol{\mu}_a) \tag{3.33}$$

where $\hat{\boldsymbol{M}}_a$ and $\hat{N}_a$ are estimates of $\boldsymbol{M}$ and N in (3.30) for the case of Δ_1, and $\boldsymbol{\mu}_a$ is the NN input obtained by delayed values for y_1 and u. In simulation, 4 delayed values of y_1 in (2.2) and 3 delayed values of the input, u, with time delay, $d = 0.02$ sec., are combined to construct the NN input signal, and $n_\sigma = 6$.

The adaptive law for the NN weights are the same as in [21] in which the output has a relative degree 1. Thus

$$\begin{aligned} \dot{\widehat{\boldsymbol{M}}}_a &= -\Gamma_{M_a}[(\hat{\boldsymbol{\sigma}} - \hat{\sigma}'\widehat{N}_a^T\boldsymbol{\mu}_a)e_1 P_{11} + k_a \widehat{\boldsymbol{M}}_a] \\ \dot{\widehat{N}}_a &= -\Gamma_{N_a}[e_1 P_{11}\boldsymbol{\mu}_a \widehat{\boldsymbol{M}}_a^T \hat{\sigma}' + k_a \widehat{N}_a], \end{aligned} \tag{3.34}$$

in which $\Gamma_{M_a}, \Gamma_{N_a} > 0$ are positive definite adaptation gain matrices, $k_a > 0$ is a $\sigma-$modification constant, $\hat{\boldsymbol{\sigma}} \triangleq \boldsymbol{\sigma}(\widehat{N}_a^T\boldsymbol{\mu})$, $\hat{\sigma}'$ is the Jacobian computed at the estimates, and P_{11} is obtained from the decomposition of P_a in (3.29) as follows:

$$P_a = \begin{bmatrix} P_{11} & P_{12} \\ P_{12}^T & P_{22} \end{bmatrix}, \quad P_{11} \in \mathbb{R},\ P_{22} \in \mathbb{R}^{6\times 6}. \tag{3.35}$$

However, the adaptive law in (3.34) becomes problematic when y_1 has a significant bias. In this case, the adaptive controller forces the biased measurement to track the reference model output, and leads to large deviation in position. At the same time is desirable that the NN not be overly responsive to high frequency sensor noise. Therefore, we introduce the following band-pass filtering of the error signal used to train the NN weights

$$e_f = H(s)e_1 = \frac{s}{(s+\omega_h)(s/\omega_M + 1)}e_1, \quad \omega_h = 0.05Hz,\ \omega_M = 40Hz. \tag{3.36}$$

Thus e_f is used in place of e_1 in (3.34). Figure 3.8 represents the frequency response of the added high-pass filter. The following parameters are used for the adaptive law in (3.34)

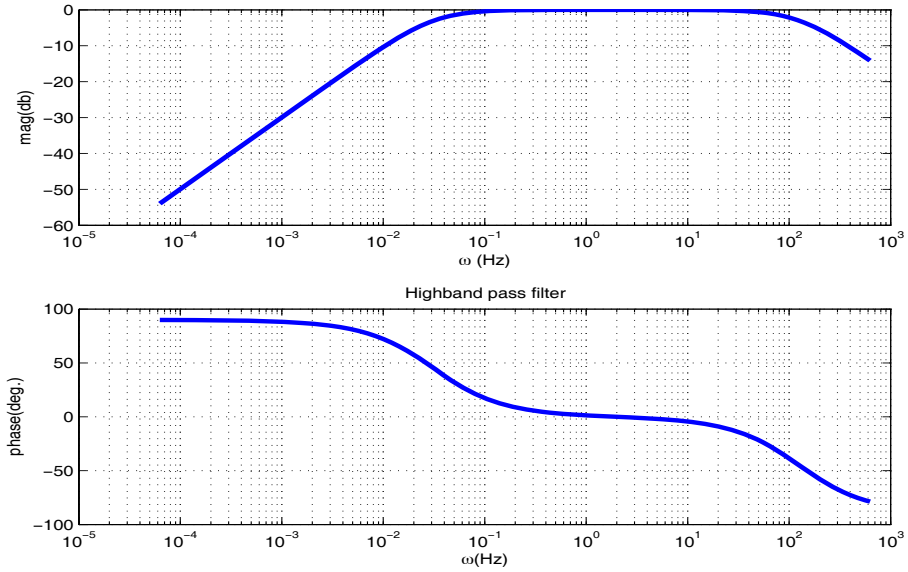

Figure 3.8: Frequency response of the highband-pass filter

$$\Gamma_{M_a} = 300I,\ \Gamma_{N_a} = 300I,\ k_a = 1, \tag{3.37}$$

where I represents the identity matrix with a compatible dimension. In implementation, the adaptive signal is also filtered through $H(s)$. Therefore, the signal v_{nn} is designed as

$$v_{nn} = H(s)[\widehat{\boldsymbol{M}}_a^T \sigma(\widehat{N}_a^T \boldsymbol{\mu}_a)], \tag{3.38}$$

leading to the following u_{ad_a} for the inner-loop acceleration controller

$$u_{ad_a} = -\frac{1}{s}[v_{nn} + v_{dc}] = -\frac{1}{(s+\omega_h)(s/\omega_M + 1)}[\hat{\boldsymbol{M}}_a^T \sigma(\hat{N}_a^T \boldsymbol{\mu}_a)] - \frac{1}{s} v_{dc}. \tag{3.39}$$

3.5 Simulation Results

In simulations, the reference command, x_c, is set to zero. As Figure 3.5 suggests, the unmodelled dynamics have a small influence on overall stability and performance. The accelerometer bias for y_1 is set at 0.001 m/sec (102 μ g). Figure 3.9 shows the acceleration response, y_1, when the base excitation is $\ddot{x}_o = 16\mu g \sin(2\pi \times 0.067t)$. The

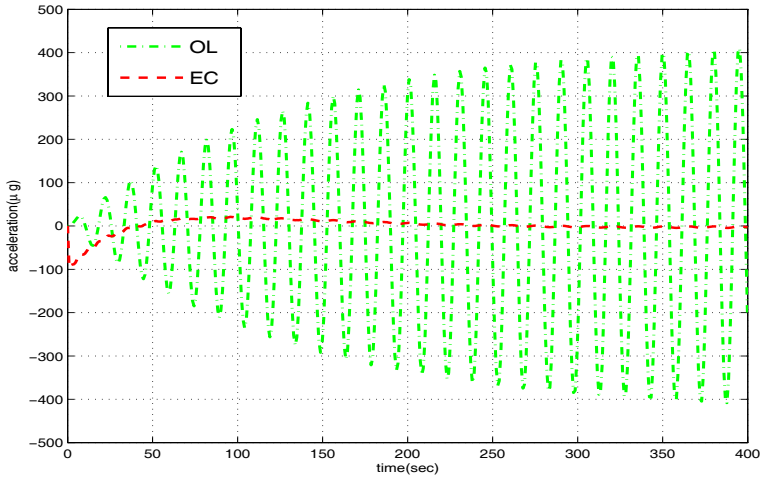

Figure 3.9: Time responses of y_1 with and without the acceleration control

base excitation frequency corresponds to the first flexible mode in the open-loop system in Figure 3.1(c), thus the open-loop system ("OL") exhibits greatly amplified responses ($|G_{b2a}(j\omega)|_{\omega=0.067Hz} \simeq 25dB$) to the given base excitation. With the existing control system ("EC"), the transmissibility is -20 dB as shown in Figure 3.5(a), and the acceleration is significantly attenuated.

When the NN is implemented with its weights being updated as in (3.34) ("NN without HP"), the vibration is further suppressed, however the isolated platform exhibits a drastic deviation in its position as shown in Figure 3.10(b). Figure 3.10(a) shows that when the highband-pass filter in (3.36) is introduced, the relative position is regulated at the same level as the existing control system. Figure 3.11 shows the effect of the highband-pass filter in (3.36) in tracking error. Without the highband-pass filter, the acceleration integral controller keeps integrating the bias even when the true acceleration perfectly matches that of the inner-loop reference model. This keeps the true acceleration from tracking the output of the inner-loop reference model as shown in Figure 3.11(a). In contrast, the highband-pass filter keeps the NN from seeing the sensor bias as tracking error by removing the bias effect in the teaching signal, and this forces the true acceleration to track the output of the inner-loop reference model as shown in Figure 3.11(b).

Assessment of isolation performance throughout the specified frequency range requires the development of a performance measure that quantifies how much the transmitted acceleration is attenuated in a nonlinear system. In this example, steady-state responses are recorded after the transient responses decay, and the attenuation

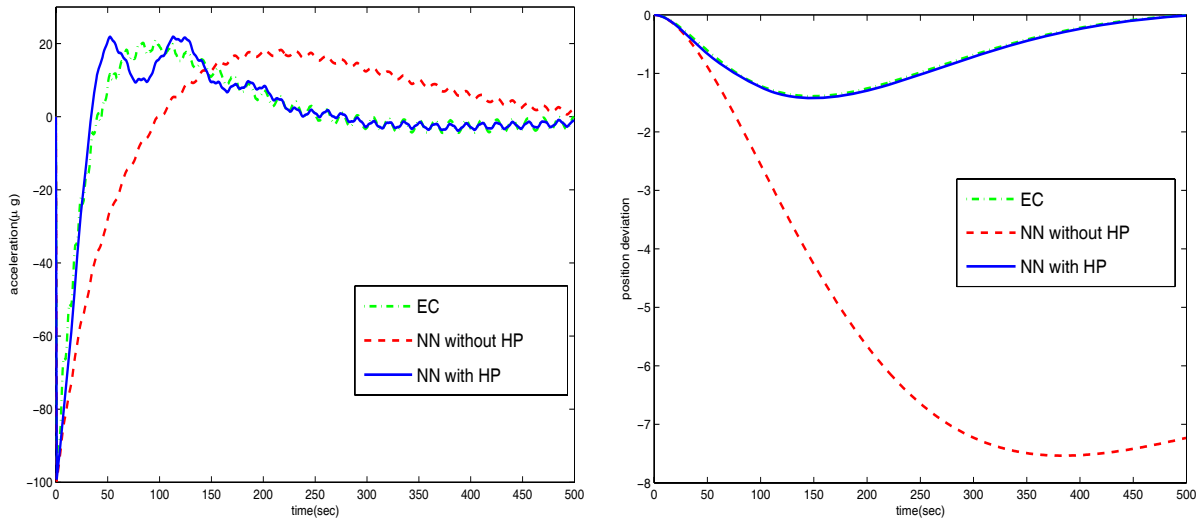

(a) Time Response of the Acceleration y_1

(b) Time Response of the Position y_2

Figure 3.10: Acceleration and Position Responses with the 0.067 Hz base excitation

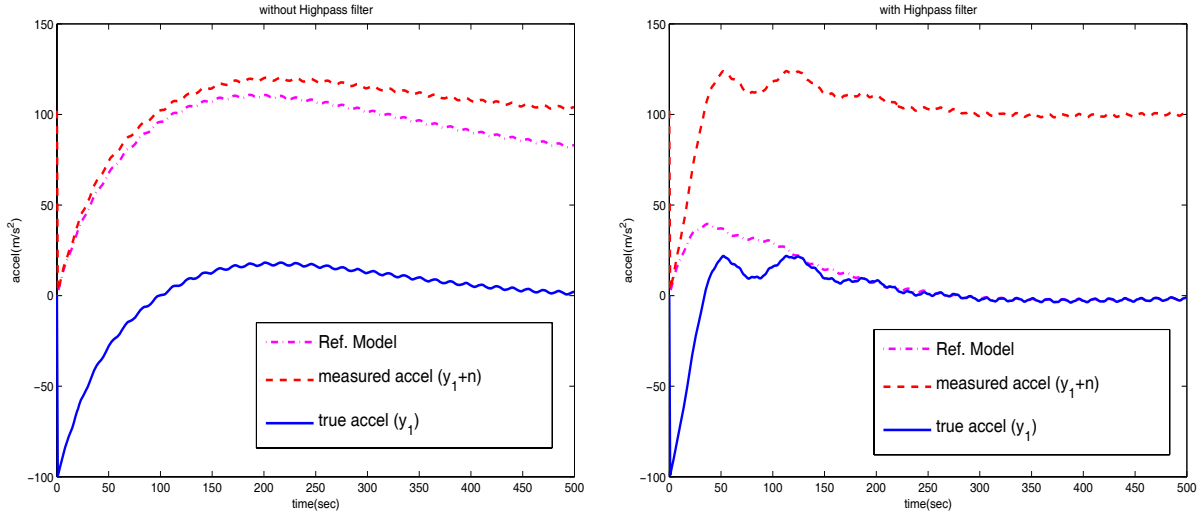

(a) The acceleration responses without the highband-Pass Filter

(b) The acceleration responses with the highband-pass filter

Figure 3.11: Responses of Inner-loop reference model, the true acceleration, and the biased acceleration

level similar to Figure 3.5(a) are found by extrapolating the recorded data. The base excitation ranges from $1.6\mu g$ to $1.6 \times 10^3 \mu g$ following the predicted ISS acceleration environment in Figure 1.1(a). The result is plotted in Figure 3.12. According to the attenuation requirement in Figure 1.1(b), active isolation is only required

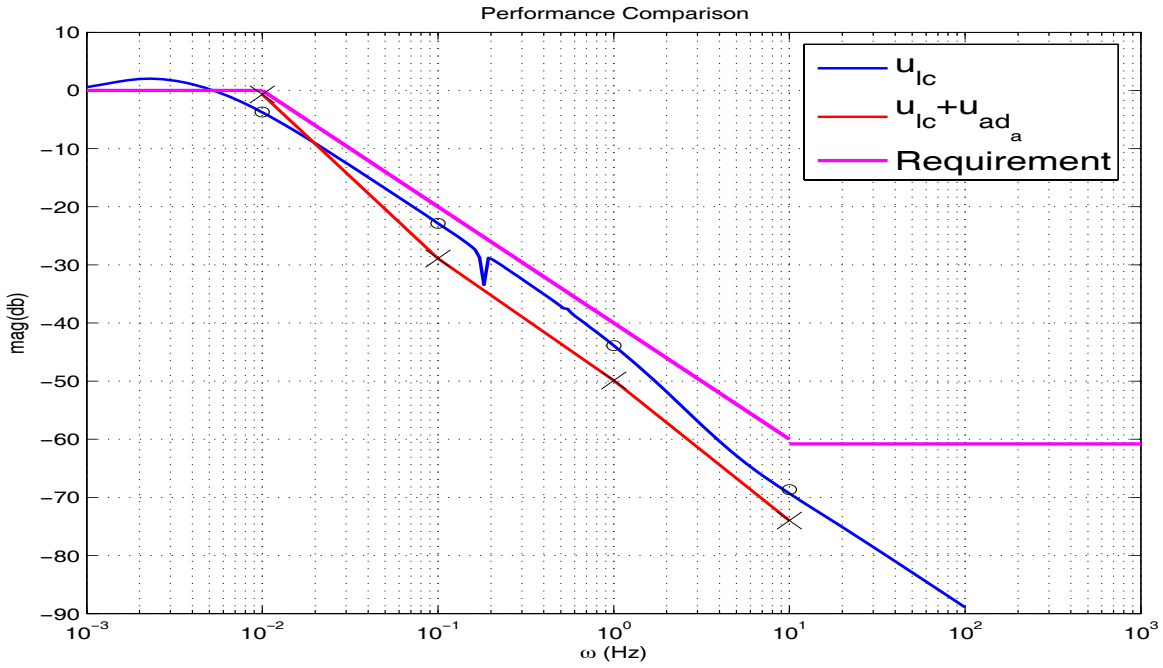

Figure 3.12: Comparison of isolation performance with and without adaptive control

over the frequency range 0.01 Hz-10 Hz because base excitations below 0.01 Hz must be transmitted to the isolated platform in order for the isolated system to move with the vehicle, and the open-loop system satisfies the performance requirement above 10 Hz. Figure 3.12 show that the adaptive controller (" $u_{lc} + u_{ad_a}$ ") outperforms the existing control system ("u_{lc}") throughout the frequency range of 0.01 Hz-10 Hz. That is, the adaptive control system promises its main benefits in the critical frequency range in which parametric uncertainties related to the inertia properties and the umibilical stiffness are expected to change the shape of the frequency responses shown in Figure 3.1. For example, the flight-test results in [3] show that the linear design fails to meet the performance requirement in the range of 0.04 Hz-0.4 Hz due to the hysteresis in the umbilical stiffness. The present results suggest that with adaptive augmentation the linear controller may be able to meet these requirements.

Investigating the frequency responses of $\frac{y_1}{d_1}$, $\frac{y_1}{d_2}$, and $\frac{y_1}{d_3}$ in Figures 3.5(b), 3.5(c), and 3.5(d) reveals that at higher frequencies (above 1 Hz), the external disturbance d_1 is most influential (-30dB) among the external disturbances d_1, d_2, and d_3, which could arise when the experiment mounted on the isolated platform has its own source of vibration. Disturbances d_2 and d_3 lead to -40dB gain over almost all frequencies, and thus are negligible disturbance sources. Figure 5.8 shows the acceleration responses when disturbances $d_1 = 160\mu g \sin(2\pi \times 0.1t)$ (0.1 Hz) and $d_1 = 480\mu g \sin(2\pi \times 1t)$ (1 Hz) are applied. Similarly as in the case of the base excitation, adaptive control generally improves performance of the existing control system between 0.1 Hz and 10 Hz as shown in Figure 3.14.

3.6 Conclusions

In this section we considered adaptive control augmentation of an existing controller for g-LIMIT. The existing control system consists of a high-gain PI acceleration controller and a low-gain PID position controller, and the

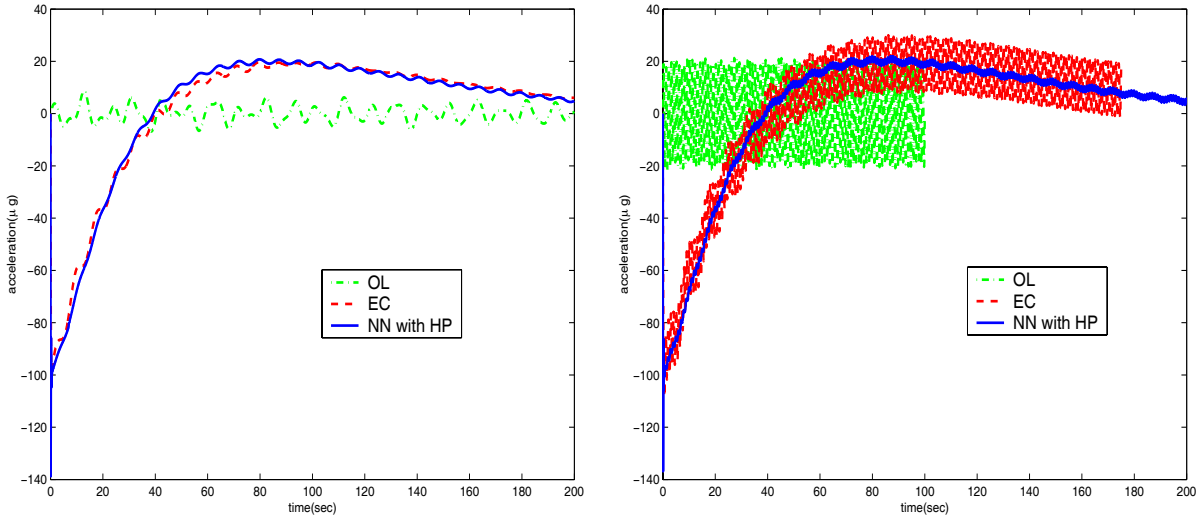

(a) The Acceleration Response with $d_1 = 160\mu g \sin(2\pi 0.1(Hz)t)$

(b) The Acceleration Responses with $d_1 = 480\mu g \sin(2\pi 1(Hz)t)$

Figure 3.13: Acceleration Responses with Direct Disturbance d_1

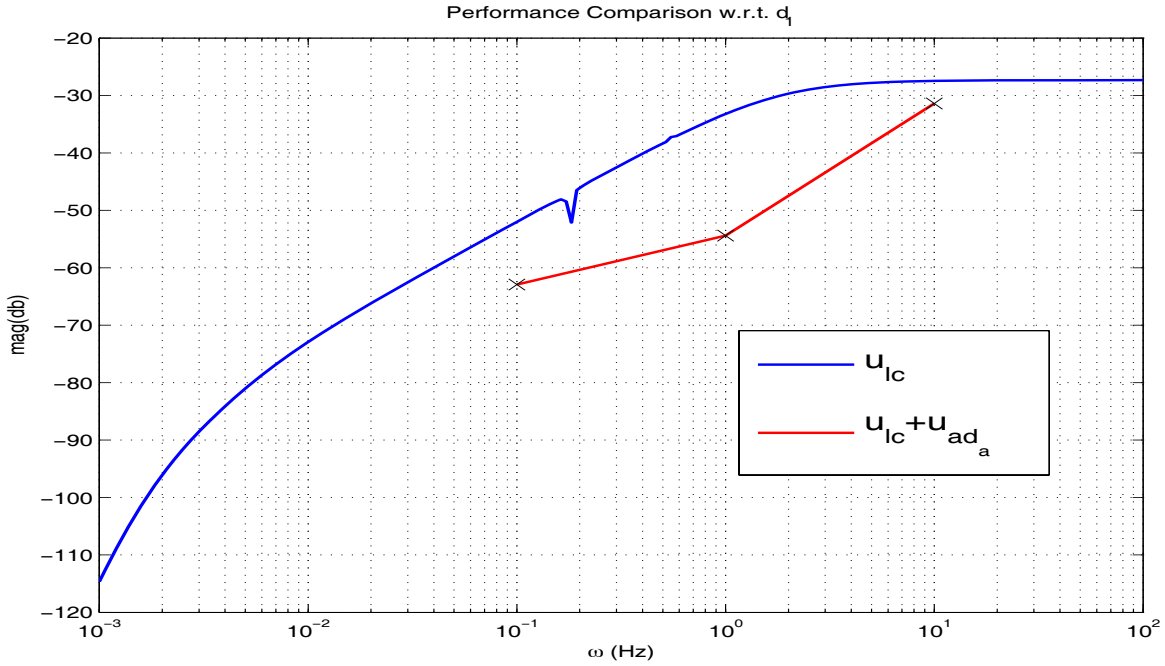

Figure 3.14: Comparison of isolation performance with and without adaptive control

acceleration controller control loop is augmented with an adaptive element. Introducing a high-pass filter for the NN teaching signal allows the NN to adapt only to the high-frequency dynamics and to ignore the effect of accelerometer bias. This permits adaptation to unmodeled dynamics while not interfering with performance of the outer loop controller in removing the effect of accelerometer bias. The adaptive control system outperforms the existing control system in the range of 0.1 Hz and 10 Hz and achieves the same level of performance over other frequencies with both base excitations and direct disturbance forces applied to the experiment.

Section 4

Inner-loop Adaptive Control for the Non-collocated Control Problem

When the sensor and actuators are configured in a collocated manner as in Section 3, the existing control system is robust to varying inertia properties and control parameters. Therefore, in this section, we investigate the robustness feature in a non-collocated setting, which is in general more challenging than a collocated problem.

4.1 Analysis of Existing Control system

When the accelerometer is located at M_3, the two measured outputs are given in (2.3), and $\boldsymbol{c}_1$, D_u, and D_d in (2.4) are

$$\boldsymbol{c}_1^T = \begin{bmatrix} 0 & 0 & -\frac{K_2}{M_3} & -\frac{C_2}{M_3} & \frac{K_3}{M_3} & \frac{C_3}{M_3} \end{bmatrix},\ D_u = 0,\ D_d = \begin{bmatrix} 0 & \frac{1}{M_3} & 0 \end{bmatrix}. \tag{4.1}$$

The parameter values are: $M_1 = 17.8488$, $C_1 = 0.5242$, $K_1 = 6.1574$, $M_2 = 20$, $M_3 = 5$, $M_4 = 15$, $C_2 = 1\times10^{-17}$, $C_3 = 1 \times 10^{-17}$, $K_2 = 15$, and $K_3 = 5$.

The plant model is required to match the relative degree 2 of the true plant in (2.4), and is assumed to consist of two mass-spring-dampers

$$\begin{aligned} \hat{M}_1(\ddot{x}_o + \ddot{x}_1) + \hat{C}_1\dot{x}_1 + \hat{K}_1x_1 - \hat{C}_2\dot{x}_2 - \hat{K}_2x_2 &= u + d_1, \\ \hat{M}_2(\ddot{x}_o + \ddot{x}_1 + \ddot{x}_2) + \hat{C}_2\dot{x}_2 + \hat{K}_3x_2 &= d_2, \end{aligned} \tag{4.2}$$

where $\hat{M}_1 = 17.8488$, $\hat{C}_1 = 0.5242$, $\hat{K}_1 = 6.1574$, $\hat{C}_2 = 1 \times 10^{-5}$, and $\hat{K}_2 = 5$. With the outputs corresponding to those in (2.2) and by letting $x_m = [x_1,\ \dot{x}_1,\ x_2,\ \dot{x}_2]^T$, the plant model is expressed in the state-space form

$$\begin{aligned} \dot{\boldsymbol{x}}_m &= A_m\boldsymbol{x}_m + \boldsymbol{b}_m(u + d_1) + \boldsymbol{b}_{m_f}\ddot{x}_o + \boldsymbol{b}_{m_d}\bar{\boldsymbol{d}}_2, \quad \boldsymbol{x}_m \in \mathbb{R}^{4\times1} \\ y_{m_1} &= \boldsymbol{c}_{m_1}^T\boldsymbol{x}_m + D_{m_d}d_2, \\ y_{m_2} &= \boldsymbol{c}_{m_2}^T\boldsymbol{x}_m. \end{aligned} \tag{4.3}$$

where $\bar{\boldsymbol{d}}_2 = [d_1\ d_2]^T$, and

$$\begin{aligned} A_m &= \begin{bmatrix} 0 & 1 & 0 & 0 \\ -\frac{\hat{K}_1}{\hat{M}_1} & -\frac{\hat{C}_1}{\hat{M}_1} & \frac{\hat{K}_2}{\hat{M}_1} & \frac{\hat{C}_2}{\hat{M}_1} \\ 0 & 0 & 1 & 0 \\ \frac{\hat{K}_1}{\hat{M}_1} & \frac{\hat{C}_1}{\hat{M}_1} & -\hat{K}_2\left(\frac{1}{\hat{M}_1} + \frac{1}{\hat{M}_2}\right) & -\hat{C}_2\left(\frac{1}{\hat{M}_1} + \frac{1}{\hat{M}_2}\right) \end{bmatrix} \\ \boldsymbol{b}_m &= \begin{bmatrix} 0 \\ \frac{1}{\hat{M}_1} \\ 0 \\ -\frac{1}{\hat{M}_1} \end{bmatrix}, \boldsymbol{b}_{m_f} = \begin{bmatrix} 0 \\ -1 \\ 0 \\ 0 \end{bmatrix}, \boldsymbol{b}_{m_d} = \begin{bmatrix} 0 \\ 0 \\ 0 \\ \frac{1}{M_3} \end{bmatrix}, \boldsymbol{c}_{m_1}^T = \begin{bmatrix} 0 \\ 0 \\ -\frac{\hat{K}_2}{\hat{M}_2} \end{bmatrix}, \boldsymbol{c}_{m_2}^T = \begin{bmatrix} 1 \\ 0 \\ 0 \\ 0 \end{bmatrix}, D_{m_d} = \frac{1}{\hat{M}_2}. \end{aligned} \tag{4.4}$$

Figure 4.1 compares the frequency responses of the plant model with those of the system in (2.4). The transmissibility from the base to the experiment, $\frac{\ddot{x}}{\ddot{x}_o} = G_{b2a}(s)$, is shown in Figure 4.1(e). The control system design generally involves $G_{u2a} = \frac{y_1(s)}{u(s)}$ and $G_{u2x} = \frac{y_2(s)}{u(s)}$ which are shown in Figures 4.1(a) and 4.1(b).

The acceleration controller $G_a(s)$ in Figure 2.2 is designed as a PID controller. Unlike the collocated control system in Section 3, in which $v = \dot{u}$ is designed as a control signal, direct use of integral control renders the pole at the origin uncontrollable (the integrator pole) with the control input u. Since this is problematic, we modify the integrator as a stable filter. This also prevents the acceleration sensor bias from being integrated and resulting an infinite gain at zero frequency. The acceleration controller is designed as

$$\begin{aligned} u_{lc} =& G_a(s)\big[w_p - (y_1 + n)\big] = (K_{I_p} + \frac{K_{I_i}}{s + 0.114} + K_{I_d}\frac{s}{s/50 + 1})[w_p - (y_1 + n)], \\ =& 2700\frac{(s + 0.446)(s + 0.721)}{(s + 0.114)(s + 50)}[w_p - (y_1 + n)]. \end{aligned} \tag{4.5}$$

A root locus diagram and a bode plot for the inner-loop system, with the plant model in (4.3), are shown in Figure 4.2. The root locus diagram shows that the PID controller in (4.5) places poles of the inner closed-loop system at $-48.5, -0.73 \pm 1.44i, -0.142, -0.0034 \pm 0.023i$. In a state space form, the acceleration controller is given by

$$\begin{aligned} \dot{\boldsymbol{\eta}}_i &= A_i\boldsymbol{\eta}_i + \boldsymbol{b}_i(w_p - (y_1 + n)), \\ u_{lc} &= \boldsymbol{c}_i^T\boldsymbol{\eta}_i + D_i(w_p - (y_1 + n)). \end{aligned} \tag{4.6}$$

When the controller in (4.5) is applied to the true plant in (2.4), the resulting root-locus plot is shown in Figure 4.3(a) with the second mode zoomed in Figure 4.3(b). Due to the presence of unmodelled dynamics, as the system gain increases, the acceleration controller makes the inner closed-loop system unstable. With the gain in (4.5), the poles are located at $-45.4, -2.27 \pm 2.10i, 0.0025 \pm 0.60i, -0.0026 \pm 0.02i, -0.14$. Frequency responses for the inner closed loop system are also shown in Figure 4.4. Figure 4.4(f) shows that unlike the integral controller in (3.4), the controller in (4.5) does not induce an infinite gain at zero frequency, and results in bounded position deviation in the presence of the accelerometer bias.

The outer-loop position controller, $G_x(s)$, in Figure 2.2 is selected the same as in (3.6). Figures 4.5 and 4.6 shows the root locus diagram for the overall closed loop. Figure 4.7 shows frequency responses of the overall closed loop system for completeness. Note that since the overall closed-loop system is unstable for the true plant, frequency responses for the true plant are not as meaningful as those for the plant model.

4.2 Adaptive Control Design

The plant model in (4.3), with $d_1 = d_2 = \ddot{x}_o = n = 0$, is written in normal form as

$$\begin{aligned} \dot{\xi}_{m_1} =& \xi_{m_2} \\ \dot{\xi}_{m_2} =& \boldsymbol{a}_1^T\boldsymbol{\xi}_m + \boldsymbol{a}_2^T\boldsymbol{z}_m + b_m u \\ \dot{\boldsymbol{z}}_m =& F_1\boldsymbol{z}_m + \boldsymbol{g}_1\xi_{m_1}, y_{m_1} = \xi_{m_1}, \end{aligned} \tag{4.7}$$

where $\boldsymbol{\xi}_m = [\xi_{m_1}\ \xi_{m_2}]^T$, $\boldsymbol{z}_m \in \mathbb{R}^{2\times 1}$, and a_1, a_2, F_1, G_1 can be obtained from the system matrices in (4.3). With a slight abuse of notation, letting $\boldsymbol{x}_m = [\boldsymbol{\xi}_m^T, \boldsymbol{z}_m^T]^T$, leads to a state space form for the system in (4.7)

$$\begin{aligned} \dot{\boldsymbol{x}}_m =& A_n\boldsymbol{x}_m + \boldsymbol{b}_n u \\ y_{m_1} =& \boldsymbol{c}_n^T\boldsymbol{x}_m, \end{aligned} \tag{4.8}$$

where

$$A_n = \begin{bmatrix} \begin{bmatrix} 0 & 1 \\ \boldsymbol{a}_1^T \end{bmatrix} & \begin{bmatrix} 0 \\ a_2^T \end{bmatrix} \\ \boldsymbol{g}_1\boldsymbol{c}_n^T & F_1 \end{bmatrix}, \boldsymbol{b}_n = \begin{bmatrix} 0 \\ b_m \\ 0 \end{bmatrix}, \boldsymbol{c}_n = \begin{bmatrix} 1 \\ 0 \\ 0 \end{bmatrix}. \tag{4.9}$$

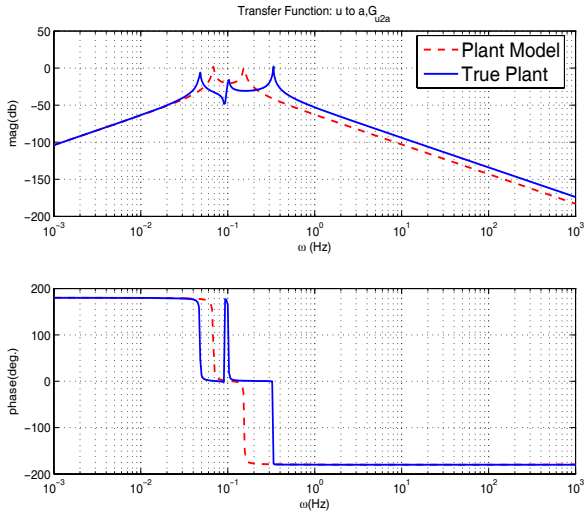

(a) Bode plot for G_{u2a} $(= \frac{y_1(s)}{u(s)})$.

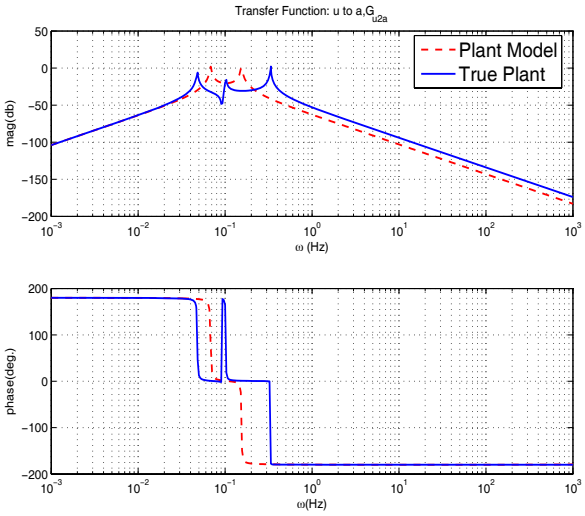

(b) Bode plot for G_{u2x} $(= \frac{y_2(s)}{u(s)})$.

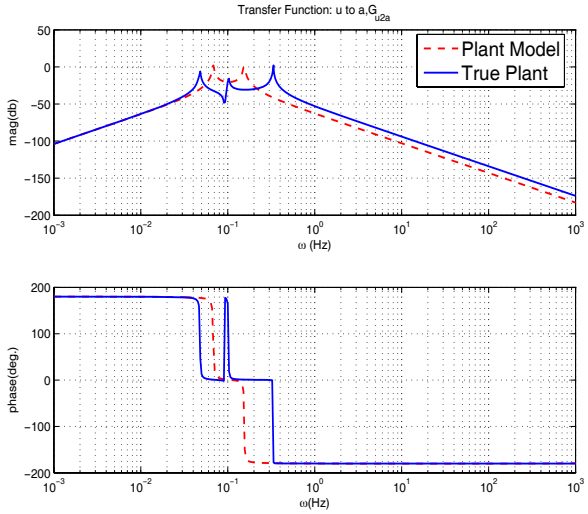

(c) Bode plot for G_{b2a} $(= \frac{y_1(s)}{\ddot{x}_o(s)})$.

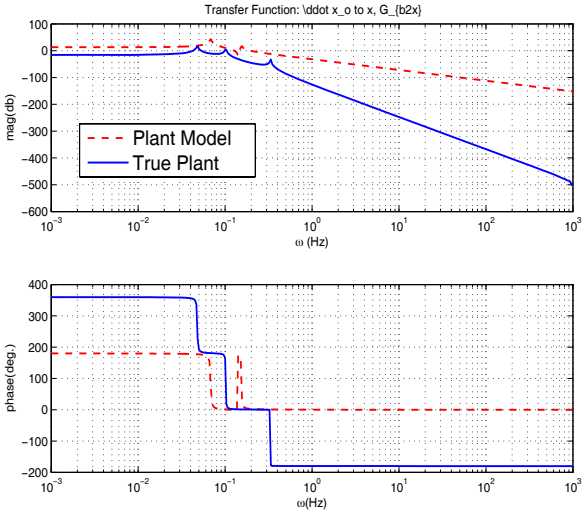

(d) Bode plot for G_{b2x} $(= \frac{y_2(s)}{\ddot{x}_o(s)})$.

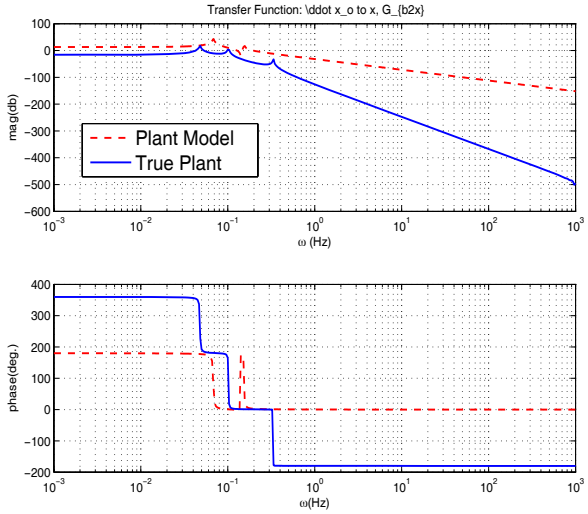

(e) Bode plot for $G_{d_1 2a}$ $(= \frac{y_1(s)}{d_1(s)})$.

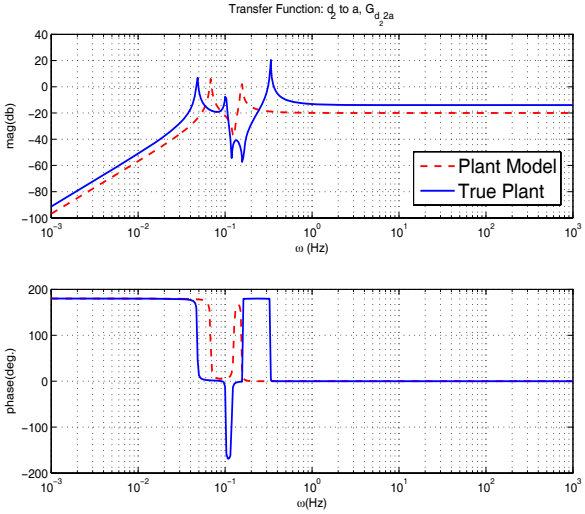

(f) Bode plot for $G_{d_2 2a}$ $(= \frac{y_1(s)}{d_2(s)})$.

Figure 4.1: Frequency response of various transfer functions for the non-collocated system

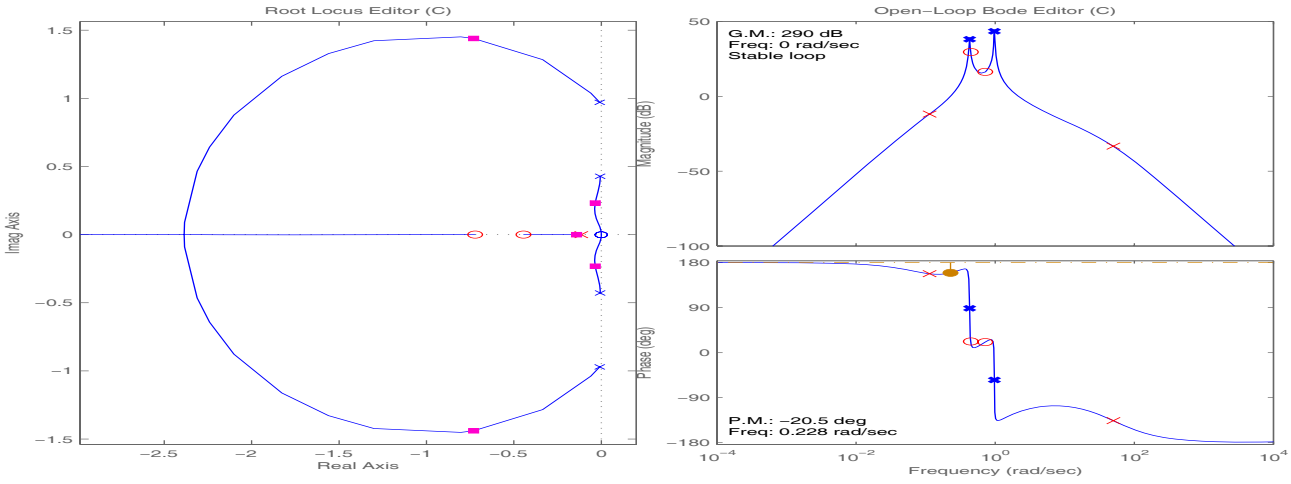

in

Figure 4.2: Root locus for the inner-loop of the plant model

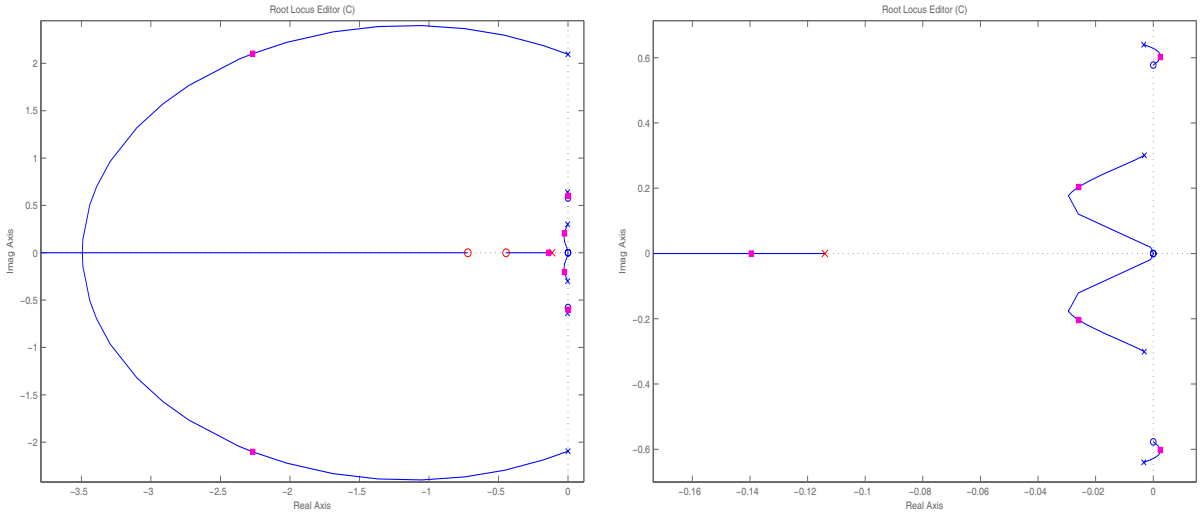

(a) Root locus for the true plant

(b) Zoomed plot for the second flexible mode

Figure 4.3: Root locus for the inner-loop of the true plant

The inner-loop reference model in Figure 3.6 consists of the plant model in (4.9) regulated by the PID controller in (4.6), whose dynamics are described by

$$\dot{\boldsymbol{\zeta}}_m = \bar{A}\boldsymbol{\zeta}_m + \bar{\boldsymbol{b}}_p w_p, \tag{4.10}$$

where $\boldsymbol{\zeta}_m = [\boldsymbol{\xi}_m \ \boldsymbol{\eta}_{i_m}]^T$, and

$$\bar{A} = \begin{bmatrix} A_n - \boldsymbol{b}_n D_i \boldsymbol{c}_n^T & \boldsymbol{b}_n \boldsymbol{c}_i^T \\ -\boldsymbol{b}_i \boldsymbol{c}_n^T & A_i \end{bmatrix}, \ \bar{\boldsymbol{b}}_p = \begin{bmatrix} \boldsymbol{b}_n D_i \\ \boldsymbol{b}_i \end{bmatrix}. \tag{4.11}$$

The subscript m is introduced to represent the states of the reference model.

Compared to the plant model in (4.8), the true plant in (2.4) can be written as

$$\begin{aligned} \dot{\boldsymbol{x}} =& A_n \boldsymbol{x} + \boldsymbol{b}_n (u + \Delta_1) + B_2 \boldsymbol{\Delta}_2 \\ \dot{\boldsymbol{z}}_2 =& F_{21} \boldsymbol{z}_1 + F_2 \boldsymbol{z}_2 + \boldsymbol{g}_2 \xi_1 \\ y_1 =& \boldsymbol{c}_n^T \boldsymbol{x}, \end{aligned} \tag{4.12}$$

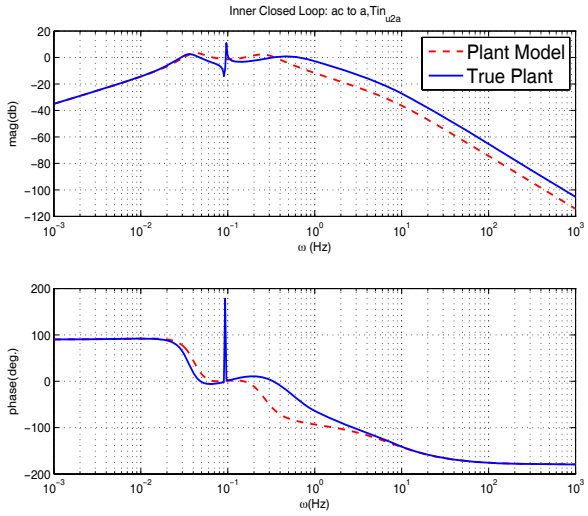

(a) Bode Plot for $\frac{y_1}{w_p}$.

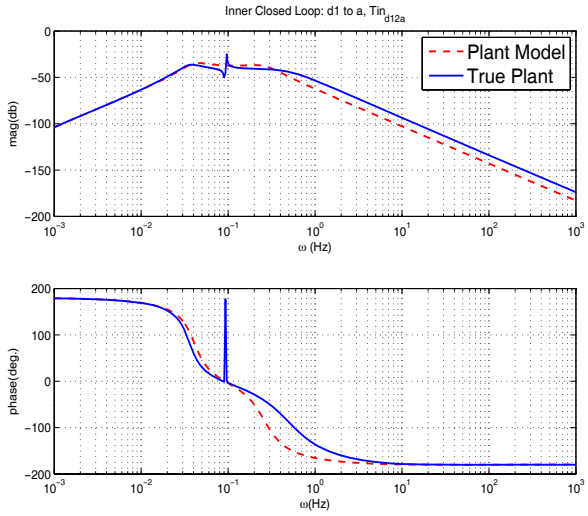

(b) Bode Plot for $\frac{y_1}{d_1}$.

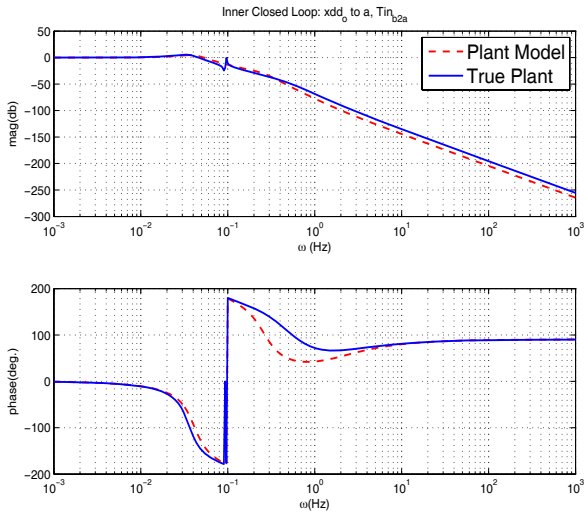

(c) Bode Plot for $\frac{y_1}{\ddot{x}_o}$.

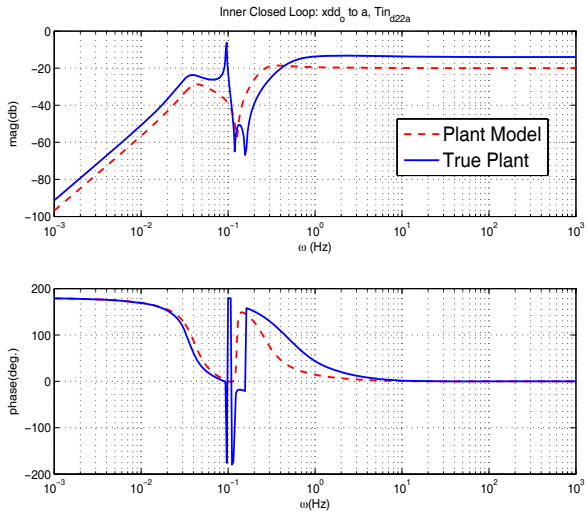

(d) Bode Plot for $\frac{y_1}{d_2}$.

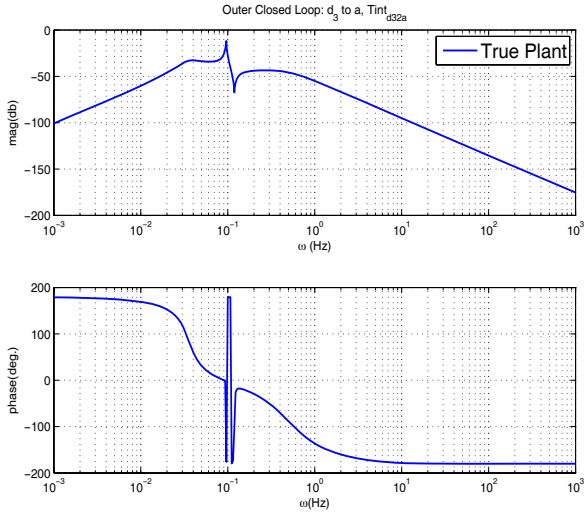

(e) Bode Plot for $\frac{y_1}{d_3}$.

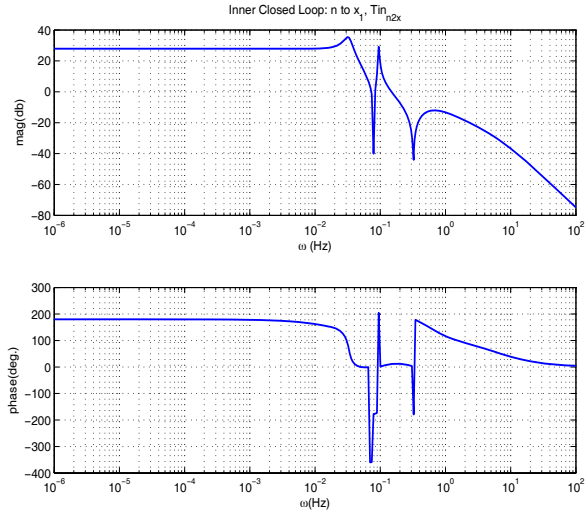

(f) Bode Plot for $\frac{y_2}{n}$.

Figure 4.4: Frequency responses for inner-loop transfer functions: the non-collocated case

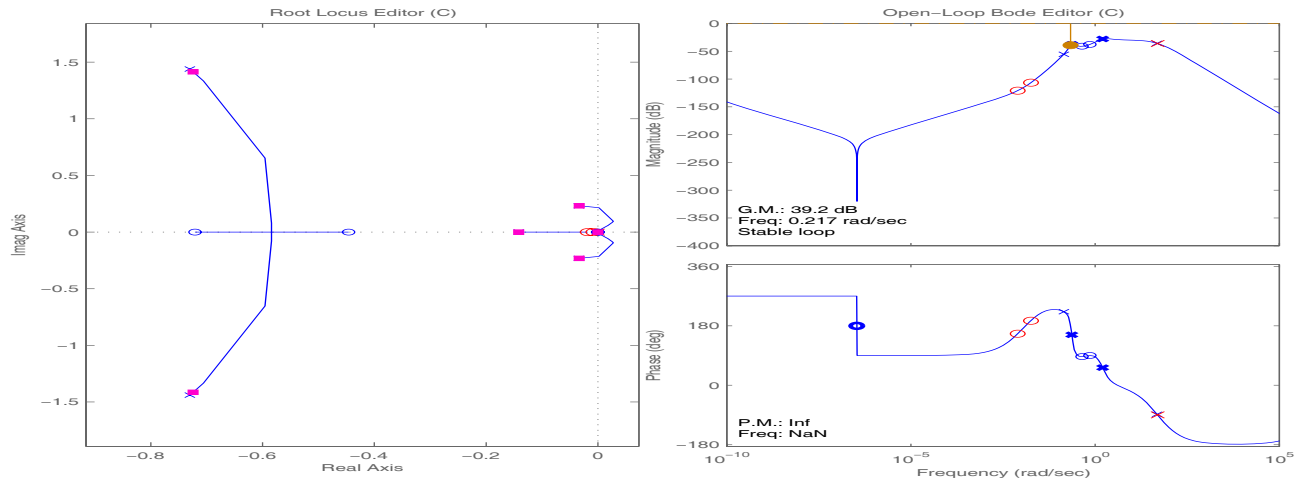

Figure 4.5: Root locus for the outer-loop of the plant model

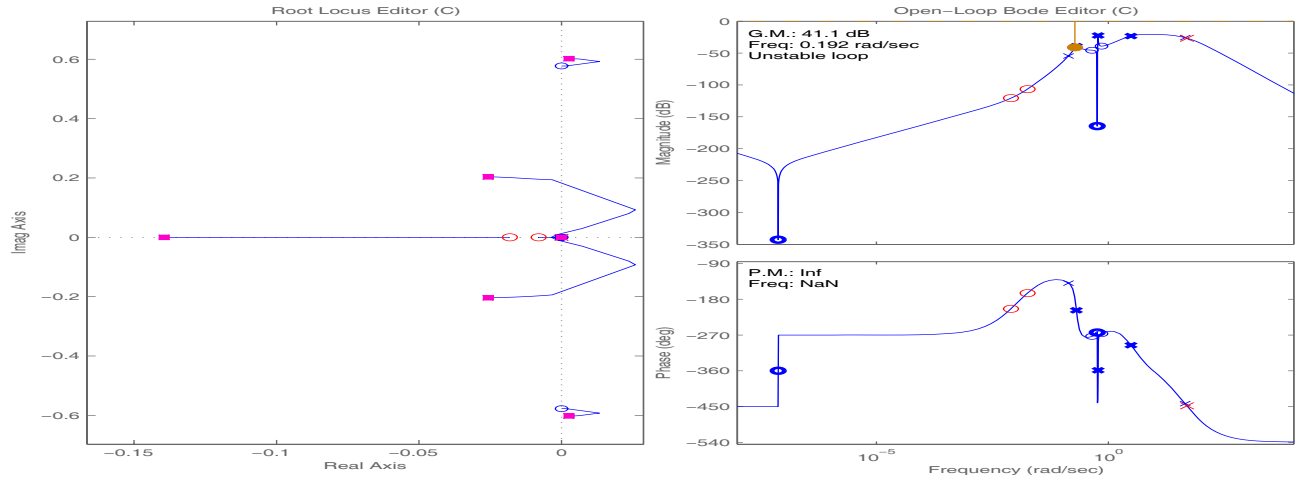

Figure 4.6: Root locus for the outer-loop of the true plant

where $\boldsymbol{x} = [\boldsymbol{\xi},\ \boldsymbol{z}_1]$ are the states that correspond to $\boldsymbol{x}_m$ in the plant model, $\boldsymbol{z}_2 \in \mathbb{R}^{2\times 1}$ represents the state of the unmodelled dynamics, $B_2 = [0\ I_{2\times 2}]^T$, and $F_{21},\ F_2,\ \boldsymbol{g}_2$ are obtained accordingly when the system in (2.4) is transformed into a normal form. The uncertainties are derived as

$$\begin{aligned}\Delta_1 =& \frac{1}{b_m}\left[\boldsymbol{c}_1^T A^2 \boldsymbol{x} + \boldsymbol{c}_1^T A \boldsymbol{b} u + \boldsymbol{c}_1^T A B_d \boldsymbol{d} + D_d \ddot{d}_2 - \boldsymbol{a}_1^T \boldsymbol{\xi} - \boldsymbol{a}_2^T \boldsymbol{z}_1 - b_m u\right] \\ \boldsymbol{\Delta}_2 =& \dot{\boldsymbol{z}}_1 - F_1 \boldsymbol{z}_1 - \boldsymbol{g}_1 \xi_1.\end{aligned} \tag{4.13}$$

Let

$$u = u_{lc} + u_{ad_a}, \tag{4.14}$$

where u_{lc} is the control signal in (4.5). Applying u_{lc} to the system in (4.12) results in the following inner-loop closed system

$$\begin{aligned}\dot{\boldsymbol{\zeta}} =& \bar{A}\boldsymbol{\zeta} + \bar{\boldsymbol{b}}_p w_p + \bar{\boldsymbol{b}}_n (u_{ad} + \Delta_1) + \bar{B}_\Delta \boldsymbol{\Delta}_2 \\ \dot{\boldsymbol{z}}_2 =& F_{21}\boldsymbol{z}_1 + F_2 \boldsymbol{z}_2 + \boldsymbol{g}_2 y_1,\end{aligned} \tag{4.15}$$

where $\boldsymbol{\zeta} = [\boldsymbol{x},\ \boldsymbol{\eta}_i]^T$, and

$$\bar{\boldsymbol{b}}_n = \begin{bmatrix} \boldsymbol{b}_n \\ 0 \end{bmatrix},\ \bar{B}_\Delta = \begin{bmatrix} B_2 \\ 0 \end{bmatrix}. \tag{4.16}$$

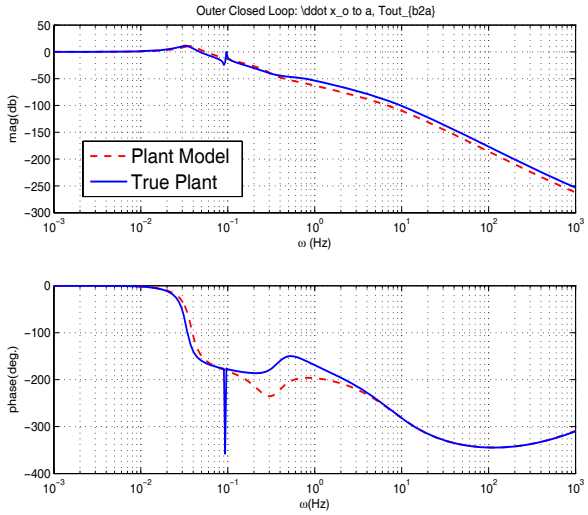

(a) Bode plot for $\frac{y_1}{\ddot{x}_o}$.

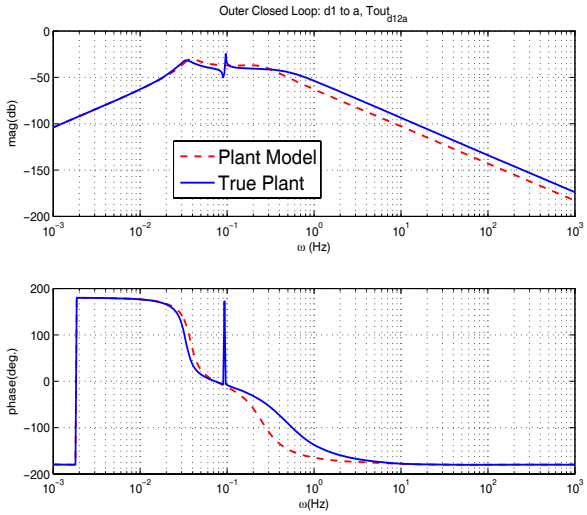

(b) Bode plot for $\frac{y_1}{d_1}$.

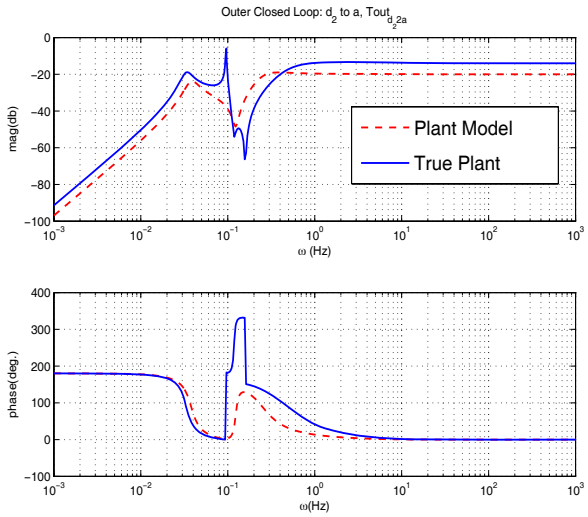

(c) Bode plot for $\frac{y_1}{d_2}$.

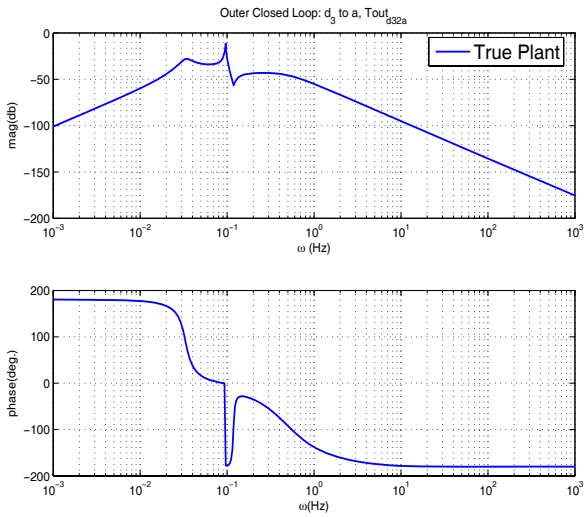

(d) Bode plot for $\frac{y_1}{d_3}$.

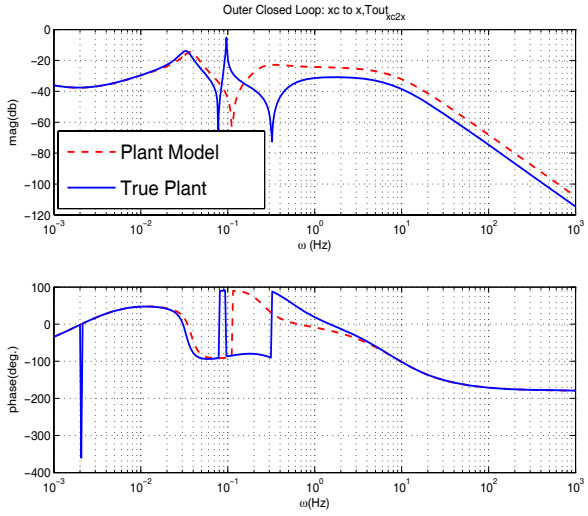

(e) Bode plot for $\frac{y_2}{x_c}$.

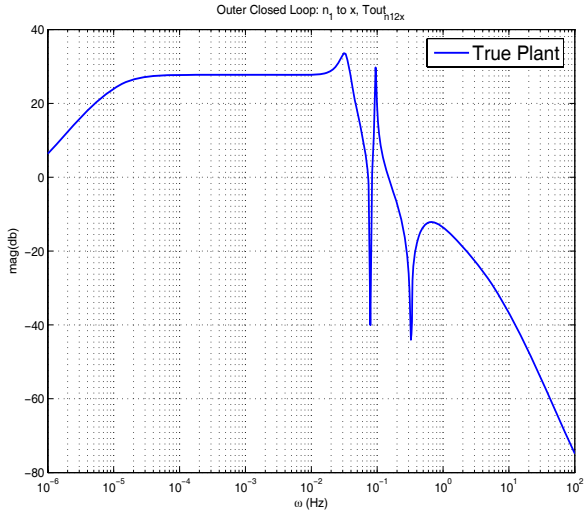

(f) Bode plot for $\frac{y_2}{n}$.

Figure 4.7: Frequency responses for overall (inner-loop+outer-loop) transfer functions

By defining the error vector as in (3.23), we can derive the following error dynamics

$$\begin{aligned}\dot{\boldsymbol{E}} =&\bar{A}\boldsymbol{E} - \bar{\boldsymbol{b}}_n(u_{ad} + \Delta_1) - \bar{B}_\Delta \boldsymbol{\Delta}_2 \\ \dot{\boldsymbol{z}}_2 =&F_{21}\boldsymbol{z}_1 + F_2\boldsymbol{z}_2 + \boldsymbol{g}_2 y_1, \\ e_1 =&y_{m_1} - y_1 = \bar{\boldsymbol{c}}_n^T \boldsymbol{E}\end{aligned} \tag{4.17}$$

where $\bar{\boldsymbol{c}}_n = \begin{bmatrix} \boldsymbol{c}_n^T & 0 \end{bmatrix}^T$.

A single hidden layer NN presented in Section 3.3 is used to approximate Δ_1. Its structure is the same as that in Section 3.4. The adaptive law for the NN are essentially the same to the one in (3.34), where P_{11} is obtained by solving for a P in (3.29) with $\bar{A}_a$ replaced by $\bar{A}$ in (4.17) and then decomposing P as in (5.23). The tuning parameters are:

$$\Gamma_{M_a} = 1000I,\ \Gamma_{N_a} = 1000I,\ k_a = 0.5 \tag{4.18}$$

The resulting control law for u_{ad} is

$$u_{ad_a} = -\widehat{\boldsymbol{M}}_a^T \sigma(\widehat{N}_a^T \boldsymbol{\mu}_a). \tag{4.19}$$

Remark 1. In this section, a linear controller in Section 3.2.3 is not introduced because $\bar{A}$ in (4.17) is Hurwitz. Such a controller can be introduced to robustify the error dynamics in (4.17). Also, the acceleration y_1 has relative degree 2 with respect to u, we apply directly the method in [11, 26] for designing an adaptive controller.

4.3 Simulation Results

Simulations are run with $x_c = 0$ and the same bias as in Section 5.3. Figure 3.9 shows the acceleration response, y_1, when the base excitation is $\ddot{x}_o = 160\mu g \sin(2\pi \times 0.067t)$. As expected, the existing control system renders the closed-loop system unstable. The adaptive controller makes the closed-loop system stable, and suppresses vibrations compared to the open loop system. Figure 4.9 shows that the control system with adaptive control

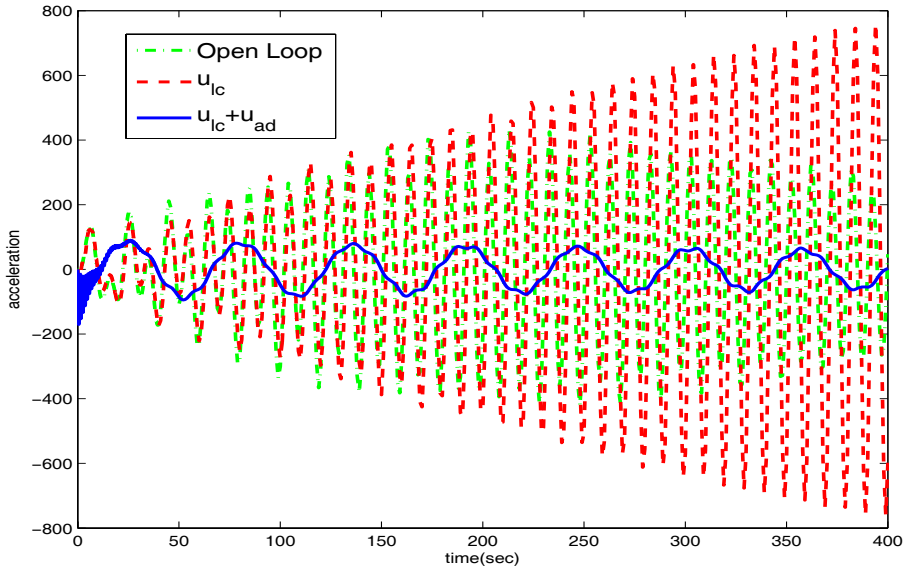

Figure 4.8: Time responses of y_1 with and without adaptive control

results in deviation in position of M_1 within the limit of 1.0 m.

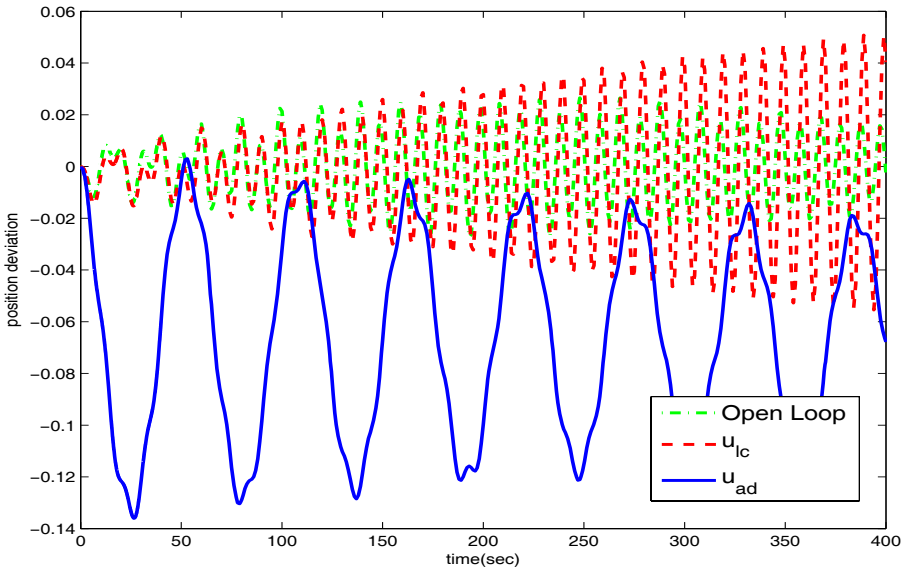

Figure 4.9: Time responses of y_2 with and without adaptive control

4.4 Conclusions

In this section we addressed the issue of robustness of the existing control system in a non-collocated configuration for g-LIMIT. Unlike the collocated control problem in Section 1, the presence of unmodelled dynamics within the bandwidth of interest may lead to an instability in the closed-loop system. The adaptive controller enhances robustness to unmodelled dynamics and recovers the stability of the nominal closed loop system.

Section 5

Inner-Loop/Outer-loop Adaptive Control for the Collocated Problem

In Sections 3 and 4, we considered augmenting the inner-loop acceleration controller by employing a single NN. By introducing a highband-pass filter for both the teaching signal for the NN and an adaptive signal, we were able to achieve that the position deviation is regulated at the same level as that for the existing control system, but with improved isolation performance (Section 3) and improved robustness in the case of non-collocated sensors (4).

In this Section, we pursue the idea of adaptively augmenting the outer loop controller as well. The goal will be to attenuate the effect of accelerometer bias, which is one of the main objectives of the existing control system design for g-LIMIT. Accelerometer bias is at the mili-g level, while the true acceleration is at the micro-g level. This bias is integrated by the integral action in the inner-loop and if not compensated will result in a large position deviation. Steady state deviation is removed by integral action in the outer loop. However, transients can result in a violation of the maximal travel distance of 1.0 m. This can be avoided by increasing the gain for the outer-loop position controller, but at the expense of degrading vibration isolation performance. Therefore the objective in adding adaptation is to improve both vibration isolation and position regulation. An immediate obstacle in this attempt is that only a single control is available while two outputs are to be regulated. Therefore, to overcome this difficulty we take advantage of the frequency separation between acceleration and position isolation requirements. Also, since adaptive control is introduced to both the inner-loop and the outer-loop, a reference model required to derive the error dynamics is constructed by considering both the acceleration controller and the position controller shown in Figure 2.2.

5.1 Analysis of the Existing Control System

With the goal of adaptive control augmentation in mind, we first provide an analysis of the closed-loop system n the absence of modelling uncertainty and external disturbances, i.e., $\ddot{x}_o = d_1 = 0$ in (3.3). Unlike the inner-loop reference model in Sections 3 and 4, this closed-loop system consists of the plant model regulated by both the inner-loop and outer-loop controllers and will ultimately be used as a reference model when introducing the adaptive controller. With dynamic extension, $\dot{\eta} = v, \eta = u$, the system in (3.3) is rewritten as in (3.10). By defining $\boldsymbol{\xi}_m = [\xi_{m_1}\ \xi^1_{m_2}\ \xi^2_{m_2}]^T = [y_{m_1},\ y_{m_2}, \dot{y}_{m_2}]^T$, the extended system in (3.10) can be transformed into the following normal form[27]:

$$\begin{aligned} \dot{\xi}_{m_1} &= a_{11}\xi_{m_1} + \boldsymbol{a}_{12}^T\boldsymbol{\xi}_{m_2} + D_m v, \\ \dot{\boldsymbol{\xi}}_{m_2} &= A_{22}\boldsymbol{\xi}_{m_2} + \boldsymbol{b}_{22}u, \end{aligned} \tag{5.1}$$

where v and u are written as if they were independent control signals, a_{11} and $\boldsymbol{a}_{12}$ are a constant scalar and a column vector, and

$$\boldsymbol{\xi}_{m_2} = \begin{bmatrix} \xi^1_{m_2} \\ \xi^2_{m_2} \end{bmatrix},\ A_{22} = \begin{bmatrix} 0 & 1 \\ \boldsymbol{c}^T_{m_1} & \end{bmatrix},\ \boldsymbol{b}_{22} = \begin{bmatrix} 0 \\ D_m \end{bmatrix}. \tag{5.2}$$

Remark 2. We view the overall closed-loop system as a single input double output system. Therefore, the normal form in (5.1) is different from that in (3.12) in which only y_1 is treated as an output.

When the dynamically extended system in (5.1) is regulated by the acceleration PI controller in (3.4) with $n = 0$, the inner-loop PI controller can be viewed as a PD controller as shown in Figure 3.7. That is, v_{lc} $(=\dot{u}_{lc})$ can be written as

$$v_{lc} = K_{I_i}\dot{\eta}_i + K_{I_p}(\dot{w}_p - \dot{y}_{m_1}) = K_{I_i}(w_p - \xi_{m_1}) + K_{I_p}(\dot{w}_p - (a_{11}\xi_{m_1} + \boldsymbol{a}^T_{12}\xi_{m_2} + D_m v_{lc})). \tag{5.3}$$

This leads to

$$v_{lc} = -d_{\xi_1}\xi_{m_1} - \boldsymbol{d}^T_{\xi_2}\boldsymbol{\xi}_{m_2} + d_w w_p + d_{\dot{w}}\dot{w}_p, \tag{5.4}$$

where

$$d_{\xi_1} = \frac{K_{I_i} + K_{I_p}a_{11}}{1 + K_{I_p}D_m},\ \boldsymbol{d}^T_{\xi_2} = \frac{K_{I_p}\boldsymbol{a}^T_{12}}{1 + K_{I_p}D_m},\ d_w = \frac{K_{I_i}}{1 + K_{I_p}D_m},\ d_{\dot{w}} = \frac{K_{I_p}}{1 + K_{I_p}D_m}. \tag{5.5}$$

Substituting the acceleration control signal in (5.4) to (5.1) leads to

$$\begin{aligned} \dot{\xi}_{m_1} &= [a_{11} - D_m d_{\xi_1}]\xi_{m_1} + [a^T_{12} - D_m \boldsymbol{d}^T_{\xi_2}]\boldsymbol{\xi}_{m_2} + D_m[d_w w_p + d_{\dot{w}}\dot{w}_p], && (5.6)\\ \dot{\boldsymbol{\xi}}_{m_2} &= A_{22}\boldsymbol{\xi}_{m_2} + \boldsymbol{b}_{22}\left[K_{I_i}\eta_i + K_{I_p}(w_p - \xi_{m_1})\right] && (5.7)\\ \dot{\eta}_i &= w_p - \xi_{m_1}. \end{aligned}$$

Remark 3. Equations (5.6) and (5.7) reveal how the signals u_{lc} and w_p affect the acceleration and position dynamics. With $w_p = 0$, (5.6) shows that by selecting a high-gain K_{I_i}, the effect of $\boldsymbol{\xi}_{m_2}$ on the ξ_{m_1} dynamics can be reduced while the high-frequency ξ_{m_1} has little effect on the slow dynamics since the slow dynamics behave as a low pass filter. That is, in this case, the high-gain acceleration controller might be enough for suppressing vibration and centering the isolation system. However, when the accelerometer has a bias n, i.e., the term ξ_{m_1} in (5.7) is replaced by $\xi_{m_1} + n$, the bias is integrated and has a detrimental effect on the position dynamics in (5.7). This necessitates the design of w_p, the outer-loop controller, so as to reduce the effect of the accelerometer bias. However, the addition of w_p has also extraneous effects on the acceleration dynamics as shown in (5.6) and tends to degrade the performance of the acceleration controller. To minimize the effect of w_p on the acceleration dynamics, the outer-loop controller w_p is designed as a low-gain, low-bandwidth controller so that w_p and u_{lc} may be separated in bandwidths, leading to two-time scale designs for u_{lc} and w_p.

To apply w_p in (3.7) to (5.6) and (5.7), we impose the following relation

$$\dot{w}_p = \boldsymbol{c}^T_c A_c \boldsymbol{\eta}_o + \boldsymbol{c}^T_c \boldsymbol{b}_c(x_c - \xi^1_{m_2}) + D_c(\dot{x}_c - \xi^2_{m_2}), \tag{5.8}$$

which leads to

$$d_w w_p + d_{\dot{w}}\dot{w}_p = \boldsymbol{g}^T_{\eta_o}\boldsymbol{\eta}_o - \boldsymbol{g}^T_{\xi_2}\boldsymbol{\xi}_{m_2} + \boldsymbol{g}^T_{\xi_2}\begin{bmatrix} x_c \\ \dot{x}_c \end{bmatrix}, \tag{5.9}$$

where $\boldsymbol{g}^T_{\eta_o} = d_w\boldsymbol{c}^T_c + d_{\dot{w}}\boldsymbol{c}^T_c A_c,\ \boldsymbol{g}^T_{\xi_2} = \begin{bmatrix} d_w D_c + d_{\dot{w}}\boldsymbol{c}^T_c & d_{\dot{w}}D_c \end{bmatrix}$. Combining (5.9) with (5.6) and (5.7) leads to the following overall closed-loop system

$$\dot{\boldsymbol{\zeta}}_m = \bar{A}\boldsymbol{\zeta}_m + B_{x_c}\begin{bmatrix} x_c \\ \dot{x}_c \end{bmatrix}, \tag{5.10}$$

where

$$\boldsymbol{\zeta}_m = \begin{bmatrix} \xi_{m_1} \\ \boldsymbol{\xi}_{m_2} \\ \eta_i \\ \boldsymbol{\eta}_o \end{bmatrix},\ \bar{A} = \begin{bmatrix} a_{11} - D_m d_{\xi_1} & \boldsymbol{a}_{12}^T - D_m(\boldsymbol{d}_{\xi_2} + \boldsymbol{g}_{\xi_2})^T & 0 & D_m \boldsymbol{g}_{\eta_o}^T \\ -\boldsymbol{b}_{22} K_{I_p} & A_{22} - \boldsymbol{b}_{22} K_{I_p} D_c \boldsymbol{c}_{m_2}^T & \boldsymbol{b}_{22} K_{I_i} & \boldsymbol{b}_{22} K_{I_p} \boldsymbol{c}_c^T \\ -1 & -D_c \boldsymbol{c}_{m_2}^T & 0 & \boldsymbol{c}_c^T \\ 0 & -\boldsymbol{b}_c \boldsymbol{c}_{m_2}^T & 0 & A_c \end{bmatrix},\ B_{x_c} = \begin{bmatrix} D_m \boldsymbol{g}_{\xi_2}^T & \\ \boldsymbol{b}_{22} K_{I_p} D_c & 0 \\ D_c & 0 \\ \boldsymbol{b}_c & 0 \end{bmatrix}. \tag{5.11}$$

5.2 Adaptive Control Augmentation

In this section we augment both the inner-loop acceleration controller and the outer-loop position controller. The goal is to improve the level of vibration suppression, while satisfying the specification on the maximal travel distance for the position deviation.

5.2.1 Error Dynamics

As in the case for the plant model in (3.10), we extend the dynamics in (2.4) by defining $\dot{\eta} = v, u = \eta$. This leads to the extended system in (3.8) Letting $\boldsymbol{\xi} = [\xi_1\ \xi_2^1\ \xi_2^2]^T = [y_1,\ y_2,\ \dot{y}_2]^T$, $\boldsymbol{z} = [x_3, x_2 + x_4, x_5, x_6]^T$, leads to the transformation $\begin{bmatrix} \boldsymbol{\xi} \\ \boldsymbol{z} \end{bmatrix} = T_a x_a$. With this transformation, compared to (5.1), the extended system in (3.8) can be transformed into the following normal form:

$$\begin{aligned} \dot{\xi}_1 &= a_{11}\xi_1 + \boldsymbol{a}_{12}^T \boldsymbol{\xi}_2 + D_m(v + \Delta_1), \\ \dot{\boldsymbol{\xi}}_2 &= A_{22}\boldsymbol{\xi}_2 + \boldsymbol{b}_{22}(u + \Delta_2) \\ \dot{\boldsymbol{z}} &= F_z \boldsymbol{z} + G_\xi \boldsymbol{\xi} + \boldsymbol{g}_{\ddot{x}_o} \ddot{x}_o + G_d \boldsymbol{d}, \end{aligned} \tag{5.12}$$

where $\boldsymbol{\xi}_2 = [\xi_2^1\ \xi_2^2]^T$, $\boldsymbol{z}$ represent the state of the stable unmodelled dynamics, and the uncertainties Δ_1 and Δ_2 are defined by

$$\begin{aligned} \Delta_1(\boldsymbol{\xi}, \boldsymbol{z}, v, \dot{d}_1, \boldsymbol{d}, \ddot{x}_o) =& \frac{1}{D_m}[\boldsymbol{c}_{a_1}^T A_a T_a^{-1} \begin{bmatrix} \boldsymbol{\xi} \\ \boldsymbol{z} \end{bmatrix} + \boldsymbol{c}_{a_1}^T \boldsymbol{b}_a v + \boldsymbol{c}_{a_1}^T \boldsymbol{b}_{a_f} \ddot{x}_o + \boldsymbol{c}_{a_1}^T B_{a_d} \boldsymbol{d} + D\dot{d}_1 - a_{11}\xi_1 - \boldsymbol{a}_{12}^T \boldsymbol{\xi}_2 - D_m v], \\ \Delta_2(\boldsymbol{\xi}, \boldsymbol{z}, \ddot{x}_o, d_1, u) =& \frac{1}{D_m}[C_{a_1} T_a^{-1} \begin{bmatrix} \boldsymbol{\xi} \\ \boldsymbol{z} \end{bmatrix} - \ddot{x}_o + D d_1 - \boldsymbol{c}_{m_2}^T \boldsymbol{\xi}_2 - D_m u]. \end{aligned} \tag{5.13}$$

Let

$$u = u_{lc} - u_{ad_a} - u_{ad_p}, \tag{5.14}$$

where u_{lc} is given by (3.4), u_{ad_a} is an adaptive signal to compensate for Δ_1, and u_{ad_p} is an adaptive signal to compensate for Δ_2. Similarly as in (5.3) and (5.4), applying u_{lc} in (3.4) leads to

$$v_{lc} = -d_{\xi_1}\xi_1 - \boldsymbol{d}_{\xi_2}^T \boldsymbol{\xi}_2 + d_w w_p + d_{\dot{w}} \dot{w}_p + \frac{K_{I_p} D_m}{1 + K_{I_p} D_m}[v_{ad_a} - \Delta_1 + \dot{u}_{ad_p}], \tag{5.15}$$

where $v_{ad_a} = \dot{u}_{ad_a}$. Applying (5.15) to (5.12) leads to

$$\dot{\xi}_1 = [a_{11} - D_m d_{\xi_1}]\xi_1 + [\boldsymbol{a}_{12}^T - D_m \boldsymbol{d}_{\xi_2}^T]\xi_2 + D_m[d_w w_p + d_{\dot{w}} \dot{w}_p] + \overline{D}_m[-v_{ad_a} + \Delta_1 - \dot{u}_{ad_p}], \tag{5.16}$$

$$\dot{\boldsymbol{\xi}}_2 = A_{22}\boldsymbol{\xi}_2 + \boldsymbol{b}_{22}\left[K_{I_i}\eta_i + K_{I_p}(w_p - \xi_1) - u_{ad_p} + \Delta_2 - u_{ad_a}\right]. \tag{5.17}$$

$$\dot{\eta}_i = w_p - \xi_1,$$

where $\overline{D}_m = D_m(1 - \frac{K_{I_p}}{1 + K_{I_p} D_m})$.

Remark 4. Note that v_{ad_a} and u_{ad_p} are intermingled in the acceleration dynamics and position dynamics. This in general implies that v_{ad_a} and u_{ad_p} interfere with each other. One way to overcome this problem is to follow the same rationale as in the design of the existing control signals u_{lc} and w_p. The control signal v_{ad_a} is designed so that it is responsive to high frequency acceleration error, and thus should have a small effect on the low frequency position dynamics. On the other hand, u_{ad_p} is designed so that it is responsive to low frequency position error.

Using relations similar to those in (5.8) and (5.9), applying the outer-loop controller in (3.5) to (5.16) and (5.17) leads to the following overall closed-loop dynamics

$$\begin{aligned}\dot{\boldsymbol{\zeta}} &= \bar{A}\boldsymbol{\zeta} + B_{x_c}\begin{bmatrix} x_c \\ \dot{x}_c \end{bmatrix} + \underbrace{\begin{bmatrix} \overline{D}_m \\ 0 \\ 0 \\ 0 \end{bmatrix}}_{\bar{B}_v}(-v_{ad_a} + \Delta_1 - \dot{u}_{ad_p}) + \underbrace{\begin{bmatrix} 0 \\ \boldsymbol{b}_{22} \\ 0 \\ 0 \end{bmatrix}}_{\bar{B}_u}(-u_{ad_p} + \Delta_2 - u_{ad_a}) \\ \dot{\boldsymbol{z}} &= F_z\boldsymbol{z} + G_\xi\boldsymbol{\xi} + \boldsymbol{g}_{\ddot{x}_o}\ddot{x}_o + G_d\boldsymbol{d}.\end{aligned} \tag{5.18}$$

By defining the error vector as

$$\boldsymbol{E} = \boldsymbol{\zeta}_m - \boldsymbol{\zeta}, \tag{5.19}$$

comparing (5.18) to (5.10) leads to the following error dynamics

$$\begin{aligned}\dot{\boldsymbol{E}} =& \bar{A}\boldsymbol{E} + \bar{B}_v(v_{ad} - \Delta_1 - \dot{u}_{ad_p}) + \bar{B}_u(u_{ad_p} - \Delta_2 - u_{ad_a}) \\ \dot{\boldsymbol{z}} =& F_z\boldsymbol{z} + G_\xi\boldsymbol{\xi} + G_{\ddot{x}_o}\ddot{x}_o + G_d\boldsymbol{d} \\ e_1 =& y_{m_1} - y_1 = \bar{\boldsymbol{c}}_1^T\boldsymbol{E}, \\ e_2^1 =& y_{m_2} - y_2 = \bar{\boldsymbol{c}}_2^T\boldsymbol{E},\end{aligned} \tag{5.20}$$

where e_1 and e_2^1 represent available measurements, and $\bar{\boldsymbol{c}}_1^T = [1\ 0\ 0]$, $\bar{\boldsymbol{c}}_2^T = [0\ 1\ 0]$. Since $\bar{A}$ is Hurwitz, for any $Q > 0$, there exists a $P > 0$ such that

$$\bar{A}P + P\bar{A} + Q = 0. \tag{5.21}$$

The eigenvalues of the matrix $\bar{A}$ are located at $-50.0071, -13.6627, -0.0310, -0.0072 \pm 0.0068j, -0.0294$, and Q is selected as $1.5I_{6\times 6}$.

5.2.2 Adaptive Control Design

Two single hidden-layer NNs are used to approximate Δ_1 and Δ_2 in (5.13). Since we deal with two NNs, one for the inner-loop and the other for the outer-loop, as noted in Remark 3, adaptive signals v_{ad_a} and u_{ad_p} are separated in frequency. For this reason, the design for adaptive signals involves the use of a high-pass and low-pass filter.

Inner-Loop Adaptive Controller

In case of the acceleration controller, the output y_1 has a relative degree 1 with respect to the signal v. Consider the following adaptive signal used for the single NN

$$v_{ad_a} = \hat{\boldsymbol{M}}_a^T\boldsymbol{\sigma}(\hat{N}_a^T\boldsymbol{\mu}_a), \tag{5.22}$$

where $\hat{\boldsymbol{M}}_a$ and $\hat{N}_a$ are estimates of $\boldsymbol{M}$ and N in (3.30) for the case of Δ_1, and $\boldsymbol{\mu}_a$ is the NN input obtained by delayed values for y_1 and u. The NN weights are updated following (3.34), with e_1 replaced by e_f in (3.36), where P_{11} is obtained from the decomposition of P in (5.21) as follows:

$$P_a = \begin{bmatrix} P_{11} & P_{21}^T & P_{31}^T \\ P_{21} & P_{22} & P_{32}^T \\ P_{31} & P_{32} & P_{33} \end{bmatrix}, \quad P_{11} \in \mathbb{R},\ P_{22} \in \mathbb{R}^{2\times 2},\ P_{33} \in \mathbb{R}^{3\times 3}. \tag{5.23}$$

The following parameters are used for the adaptive law in (3.34)

$$\Gamma_{M_a} = 300I,\ \Gamma_{N_a} = 300I,\ k_a = 1, \tag{5.24}$$

where I represents the identity matrix with a compatible dimension. The adaptive signal is also filtered through $H(s)$ and leads to the following u_{ad_a} for the inner-loop acceleration controller

$$u_{ad_a} = -\frac{1}{s}v_{ad_a} = -\frac{1}{(s+\omega_h)(s/\omega_M+1)}[\hat{\boldsymbol{M}}_a^T\sigma(\hat{N}_a^T\boldsymbol{\mu}_a)]. \tag{5.25}$$

Outer-Loop Adaptive Controller

In case of the position controller, the output y_2 has a relative degree 2 with respect to the control u, and the approach in [11] requires an error observer for the teaching signal. In this example, the estimate for $\dot{e}_2^1$ is obtained by

$$\hat{e}_2^2 = \frac{s}{1/50s+1}e_2^1, \tag{5.26}$$

which results in the NN training signal $\hat{\boldsymbol{e}}_2 = [e_2^1\ \hat{e}_2^2]^T$. As noted in Remark 3, the adaptive signal u_{ad_p} is needed to compensate for Δ_2 in the low-frequency range. To prevent interaction with u_{ad_a}, a low-pass filter is applied to the error signal

$$\hat{\boldsymbol{e}}_l = L(s)\hat{\boldsymbol{e}}_2 = \frac{1}{s/w_l+1}\hat{\boldsymbol{e}}_2,\ w_l = 0.001Hz \tag{5.27}$$

and $\hat{\boldsymbol{e}}_l$ is used in place of $\hat{\boldsymbol{e}}_2$ as the error signal in the adaptive law for the outer-loop NN

$$\begin{aligned}\dot{\hat{\boldsymbol{M}}}_p &= -\Gamma_{M_p}[(\hat{\boldsymbol{\sigma}} - \hat{\boldsymbol{\sigma}}'\hat{N}_p^T\boldsymbol{\mu}_p)\hat{\boldsymbol{e}}_l P_{22}\boldsymbol{b}_{22} + k_p\hat{\boldsymbol{M}}]\\ \dot{\hat{N}}_p &= -\Gamma_{N_p}[\hat{\boldsymbol{e}}_l P_{22}\boldsymbol{b}_{22}\boldsymbol{\mu}_p\hat{\boldsymbol{M}}_p^T\hat{\boldsymbol{\sigma}}' + k_p\hat{N}_p],\end{aligned} \tag{5.28}$$

where P_{22} is obtained from (5.23), and $\boldsymbol{\mu}_p$ is the NN input obtained by delayed values for y_2 and u. The tuning parameters for the NN are

$$\Gamma_{M_p} = 1\times10^{-4}I,\ \Gamma_{N_p} = 1\times10^{-4}I,\ k_p = 3\times10^4. \tag{5.29}$$

The signal u_{ad_p} is also filtered through the low-pass filter in (5.27). The adaptive signal u_{ad_p} is given by

$$u_{ad_p} = L(s)[\hat{\boldsymbol{M}}_p^T\sigma(\hat{N}_p^T\boldsymbol{\mu}_p)]. \tag{5.30}$$

Figure 5.1 shows the frequency responses of the band-pass filter in (3.36) and the low-pass filter in (5.27). The overall architecture for the adaptive control augmentation is depicted in Figure 5.2, in which abbreviations are defined as follows:" TP" for the true plant in (2.4), "PM" for the plant model in (3.3) with $\ddot{x}_o = n = 0$, " BP " for the band-pass filter in (3.36), " LP " for the low-pass filter in (5.27), "NN_a " for the NN in the acceleration inner-loop, and "NN_p" for the NN in the position outer-loop.

5.3 Simulation Results

When x_c is set to zero the reference model generates $y_{m_1} = y_{m_2} = 0$ and need not be implemented. Figure 5.3 shows the acceleration response y_1 and the position response y_2 with the base excitation, $\ddot{x}_o = 16\mu g\sin(2\pi(0.067)t)$ in the absence of sensor bias. The acceleration is significantly attenuated. Figure 5.3(b) also shows that the position oscillates with a small magnitude around zero, and its magnitude is much smaller than the maximal travel distance limit 1.0 m. The situation changes when sensor bias is introduced. Figure 5.4 compares the acceleration and position responses with and without sensor bias. Note that the transient position error violates

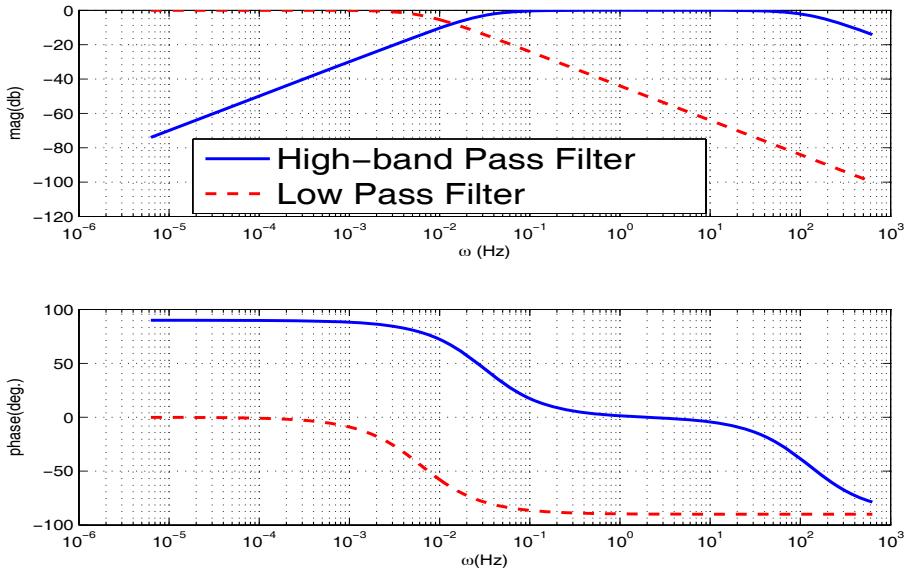

Figure 5.1: Frequency responses of filters used in adaptive control design

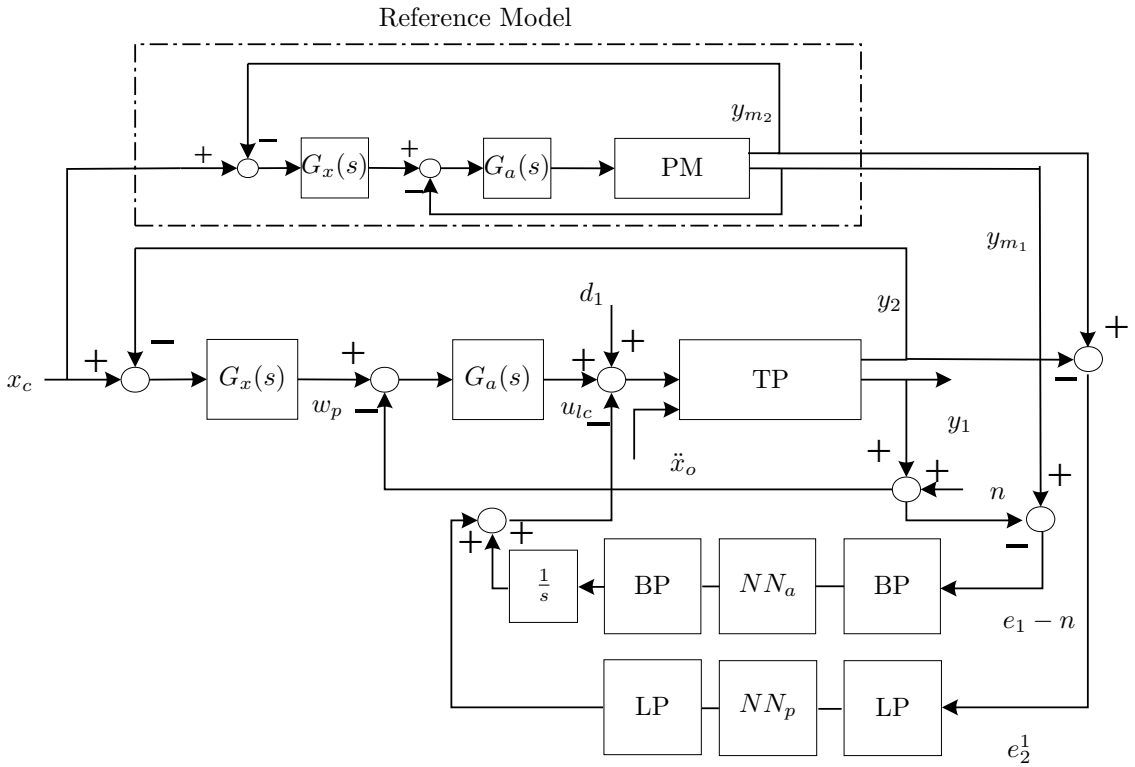

Figure 5.2: Adaptive control augmentation architecture

the 1.0 m limit. However, in steady-state, the position error converges to zero, and the same level of the acceleration is recovered as that with the existing control system without the sensor bias.

Figure 5.5 compares the acceleration and position responses when the system in (2.4) is regulated by the existing control system ("EC"), the existing control system without the outer-loop adaptive control ("EC+u_{ad_a}"), and the existing control system augmented by both the inner-loop and outer-loop adaptive controllers ("EC+u_{ad_a} +

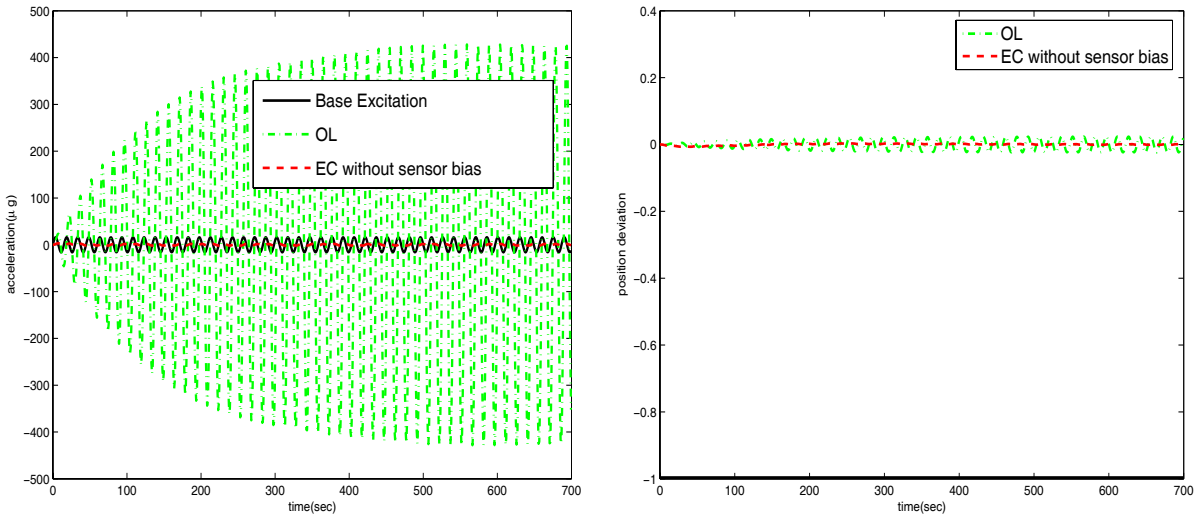

(a) Acceleration response y_1 (b) Position response y_2

Figure 5.3: Responses with the base excitation $\ddot{x} = \sin 2\pi(0.067)t$ **W**ITHOUT sensor bias

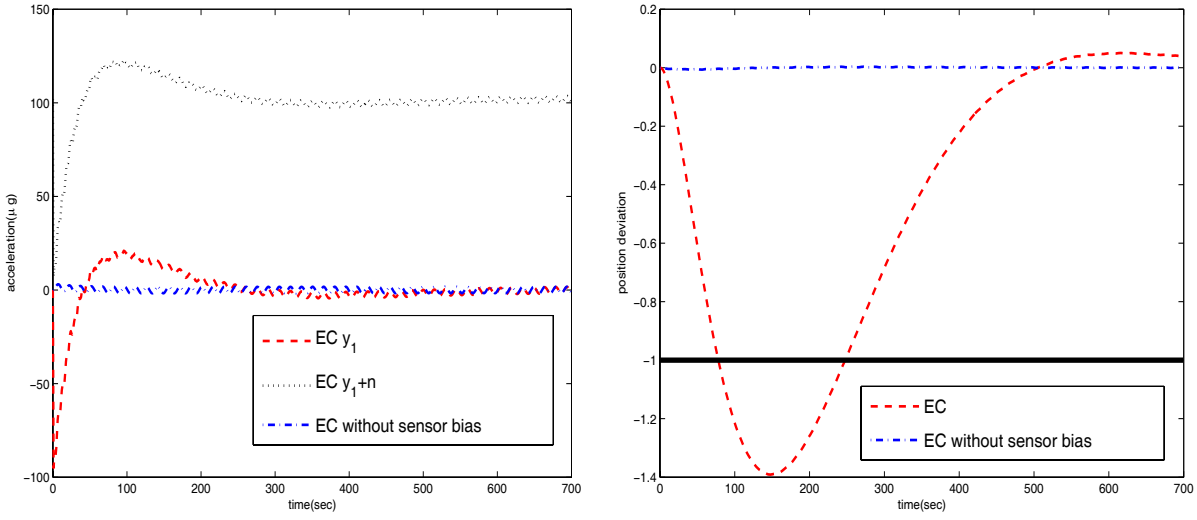

(a) Acceleration response y_1 (b) Position response y_2

Figure 5.4: Comparison of responses with the existing control system with and without accelerometer when $\ddot{x}_o = 16\mu g \sin(2\pi(0.067)t)$

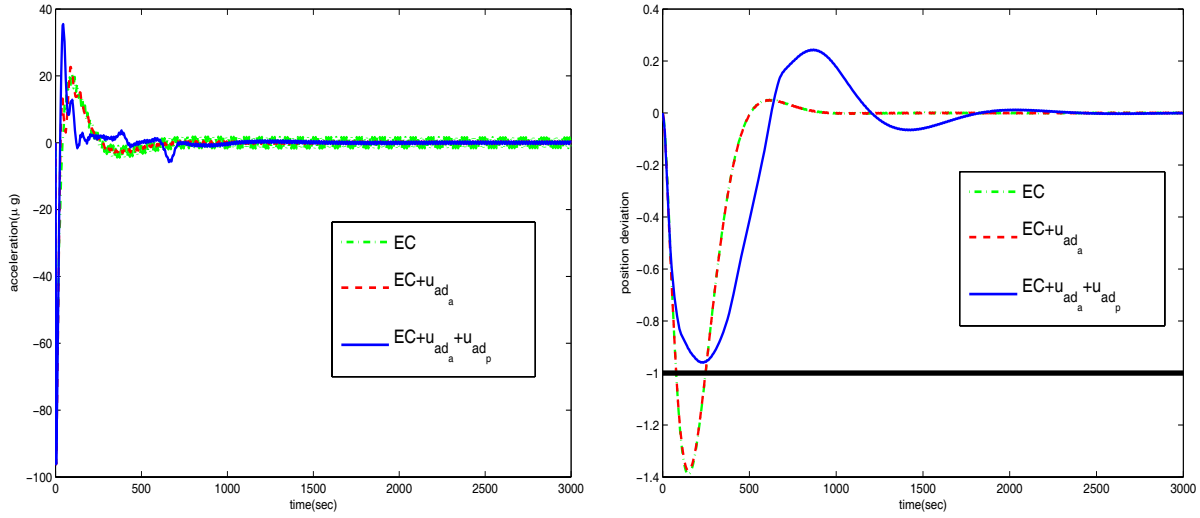

(a) Acceleration response y_1

(b) Position response y_2

Figure 5.5: Responses with the existing controller augmented by the adaptive controllers when $\ddot{x}_o = 16\mu g \sin(2\pi(0.067)t)$

u_{ad_p}") for 3000 seconds. The inner-loop adaptive controller enhances the isolation performance while the relative position is regulated at the same level as the existing control system. This indicates that the inner-loop adaptive controller is active only at high frequencies, and has little effect on the position dynamics. However, it still violates the displacement limit for the isolation system. Figure 5.5(b) shows that adding the outer-loop adaptive controller improves the response so that the limit on peak response is satisfied, with a modest increase in the peak acceleration. Figure 5.6(a) shows the transient responses for the initial 250 seconds. In the transient responses, oscillations occur at 0.05 Hz, reflecting the effect of the band-pass filter in (3.36) for the adaptive signal v_{ad_a}. Figure 5.6(b) shows that in steady-state, as the position deviation converges to zero, the effect of u_{ad_p} diminishes, and the augmented control system retains the same performance as that of the inner-loop adaptive controller without the outer-loop adaptive controller.

The overall isolation performance throughout the frequencies of interest is shown in Figure 5.7, which shows that the adaptive controller outperforms the existing control system throughout the frequency range of 0.01 Hz-10 Hz.

Figure 5.8 shows the acceleration responses when the applied disturbances are $d_1 = 16\mu g \sin(2\pi 0.1(Hz)t)$ and $d_1 = 160\mu g \sin(2\pi 5(Hz)t)$. At 0.1 Hz, $|\frac{y_1}{d_1}(j\omega)|$ is close to $-10dB$ for the open-loop system and $-50dB$ for the system regulated by the existing controller as shown in Figures 3.1(a) and 3.5(b). The existing control system is very effective in rejecting d_1 disturbances at this frequency. The adaptive controller achieves similar performance to that with the existing control system as shown in Figure 5.8(a). Figure 5.8(b) shows that at a frequency of 5.0 Hz, the adaptive controller improves the performance of the existing controller. Since $|\frac{y_1}{d_1}(j\omega)|_{\omega=5Hz}$ is close to $-30dB$ for both the open-loop system and the system with the existing controller, the acceleration responses exhibit the same magnitude of oscillation in steady-state response. With the adaptive control, the acceleration is significantly attenuated. Similarly as in the case of the base excitation, adaptive control generally improves performance of the existing control system between 0.1 Hz and 10 Hz in the presence of d_1 disturbances as shown in Figure 5.9.

Remark 5. Note that in this section the inner-loop adaptive signal u_{ad_a} and the outer-loop adaptive control signal u_{ad_p} are both designed based on the adaptive control architecture in Figure 5.2. Therefore, u_{ad_a} in this

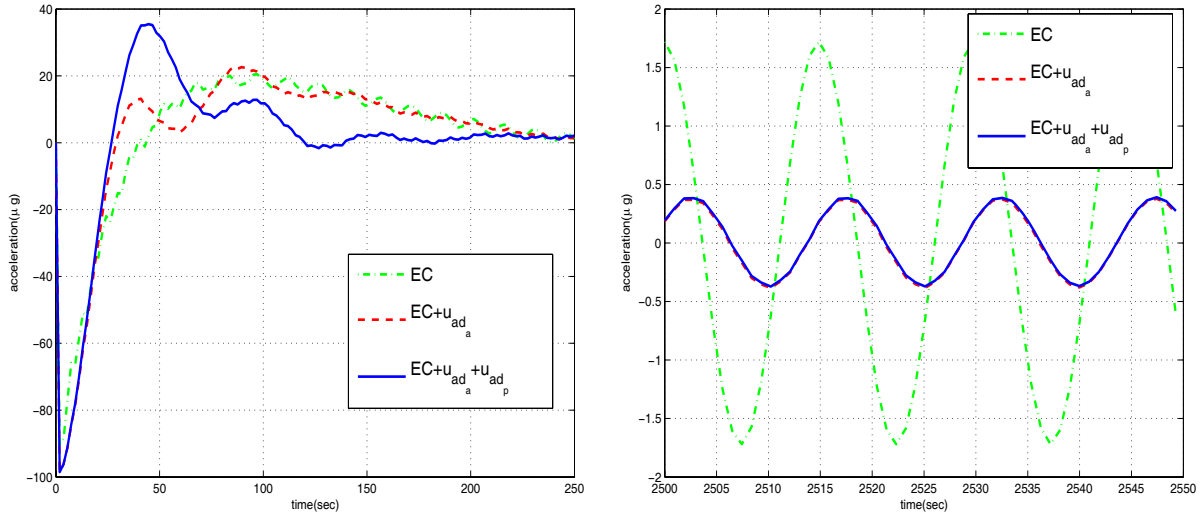

(a) Transient response y_1

(b) Steady-state response y_1

Figure 5.6: Transient and steady-state acceleration response when $\ddot{x}_o = 16\mu g \sin(2\pi(0.067)t)$

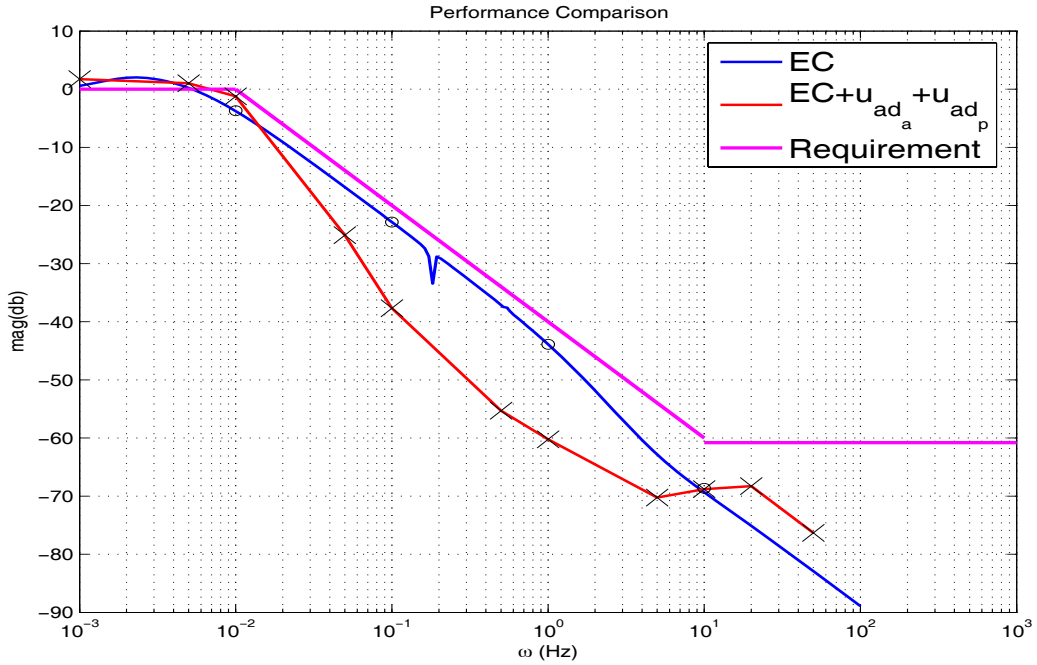

Figure 5.7: Isolation performance with the base excitations

section is different from u_{ad_a} in Sections 3 and 4, in which it is designed following the control architecture described in Figure 3.6. Figures 5.10 and 5.11 show isolation performances when the excitations come from the base ($\ddot{x}_o$) and the direct disturbance (d_1). The differences in the performance variations are mainly due to the NN parameter settings. It is interesting, however, that the adaptive control in this section is better in isolating the base excitations but is not as effective as that in Section 3 in rejecting the disturbance d_1.

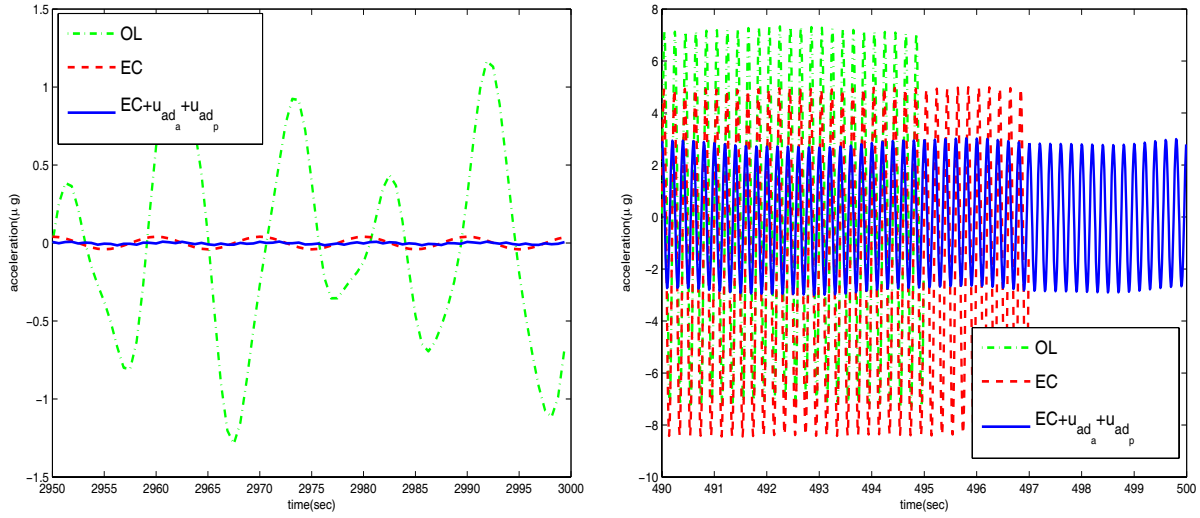

(a) Acceleration response with $d_1 = 16\mu g \sin(2\pi 0.1(Hz)t)$ (b) Acceleration responses with $d_1 = 160\mu g \sin(2\pi 5(Hz)t)$

Figure 5.8: Acceleration responses with direct disturbance d_1

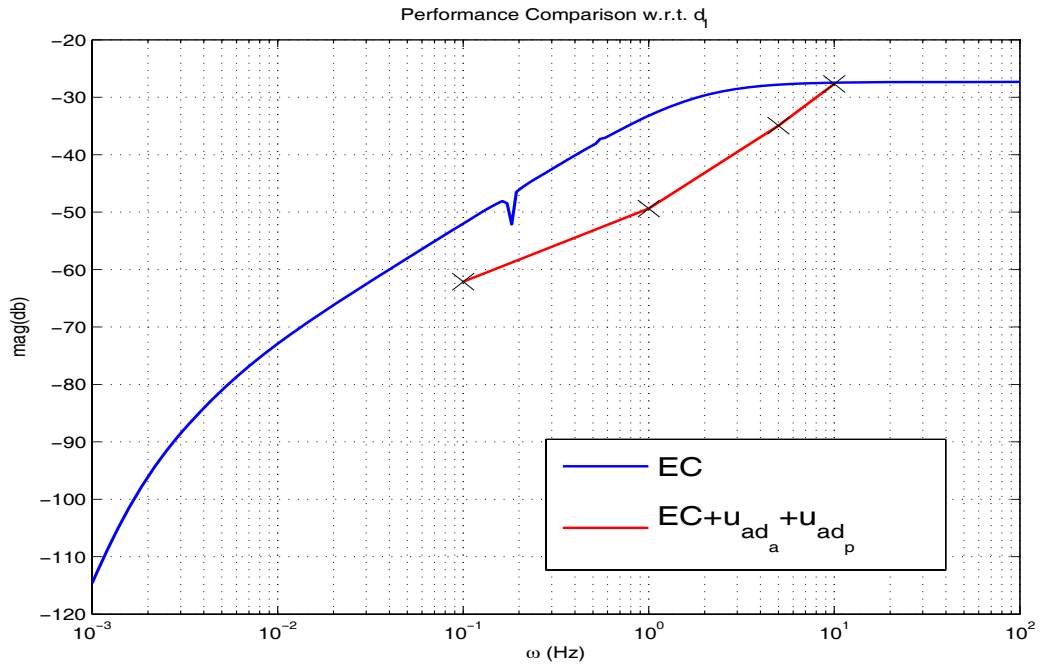

Figure 5.9: Isolation performance with the direct disturbances d_1

5.4 Conclusions

Both the acceleration control loop and the position control loop are augmented with adaptive elements that are designed based on two-time scales, similar to the approach taken in designing the existing control system. Introducing band-pass filtering of the error signals used in the adaptive laws prevents interactions between the NNs used in each loop. The adaptive control system outperforms the existing control system in the range of 0.1 Hz and 10 Hz in attenuating both the base excitation and the direct disturbance to the isolation system while meeting the specification for peak position deviation, under the same conditions that cause a violation when using the existing control design.

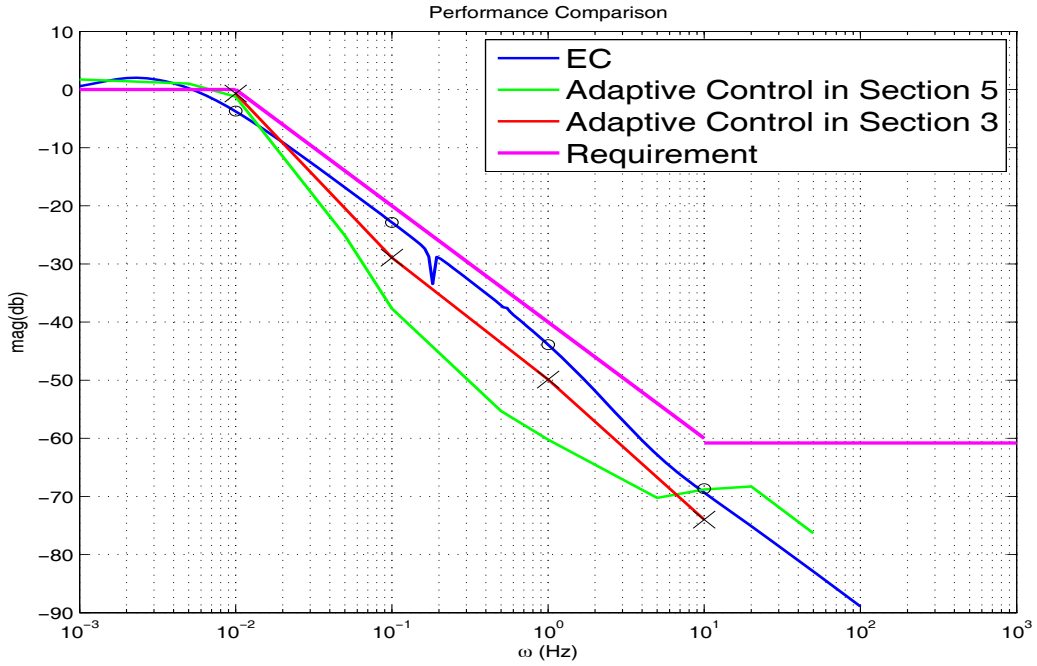

Figure 5.10: Comparison of isolation performance with the base excitations

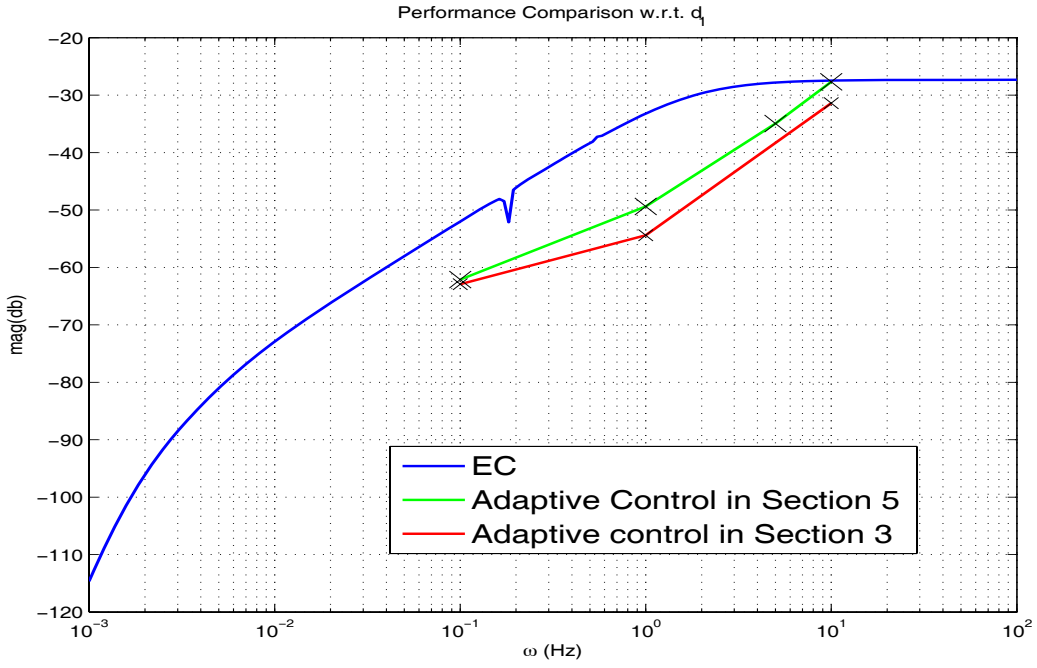

Figure 5.11: Comparison of isolation performance with the external disturbances d_1

Section 6

Conclusions and Future Extensions

In this report we have considered various aspects of augmenting a linear controller, which consists of a high-gain acceleration inner-loop controller and a low-gain outer-loop position controller, by employing adaptive neural networks in a SISO setting. Adaptive control can be augmented to improve isolation performance, robustness, and transient responses. Introducing band-pass filtering of the error signals used in the adaptive laws prevents interactions between the NNs used in each loop. The adaptive control system outperforms the existing control system in the range of 0.1 Hz and 10 Hz in attenuating both the base excitation and the direct disturbance to the isolation system.

Considering that g-LIMIT is a MIMO system in which an existing control system is independently designed for each control channel, the next step is to extend the current development to this MIMO setting. Since the existing control system is designed in a decentralized manner, it is also desirable that adaptive control be implemented in a decentralized setting as in [28]. Future research should be directed along this line leading ultimately to simulating all the degrees of freedom and implementation in a laboratory setting. In theoretical aspect, proving uniform ultimate boundedness of all the closed loop signals should be in parallel with the experimental study.

Bibliography

[1] Del Basso, S. and Bogert, P. B., "The Space Station Freedom Microgravity Environment," AIAA-1993-0831, January 1993.

[2] Bushnell, G. S., Anderson, T. M., Becraft, M. D., and Jacot, A. D., "Microgravity Performance Flight Characterization of an International Space Station Active Rack Isolation Prototype System," *AIAA/ASME/ASCE/AHS/ASC Structures, Structural Dynamics, and Materials Conference and Exhibit, 38th, and AIAA/ASME/AHS Adaptive Structures Forum*, AIAA 1997-1203, Kissimmee, FL, April 1997.

[3] Bushnell, G. S. and Becraft, M. D., "Microgravity Performance Flight Characterization of an International Space Station Active Rack Isolation Prototype System," *Proceedings of the 16th IEEE Instrumentation and Measurement Technology Conference*, Vol. 1, May 1999, pp. 260 – 267.

[4] Moss, L., Just, M., Grodsinsky, C., Heese, J., and Humphreys, B., "Microgravity Environment Predictions and Control for the Fluids Integrated Rack," *AIAA Aerospace Sciences Meeting*, AIAA 2004-5019, Reno, NV, January 2004.

[5] Kim, Y. and Whorton, M. S., "Equations of Motion for the g-LIMIT Microgravity Vibration Isolation System," Tech. Rep. NASA TM-1999-209009, January 1999.

[6] Grodsinsky, C. M. and Whorton, M., "A Survey of Active Vibration Isolation Systems for Microgravity Applications," *AIAA Journal of Spacecraft and Rockets*, Vol. 37, No. 8, Sep.-Oct. 2000.

[7] Calhoun, P. C. and Hampton, R. D., "Optimal Control Design using an H_2 Method for the Glovebox Integrated Microgravity Isolation Technology (g-LIMIT)," *Proceedings of AIAA guidance,navigation and control conference*, AIAA 2002-5020, Monterey, CA, August 2002.

[8] Jackson, M., Kim, Y., and Whorton, M., "Design and Analysis of the g-LIMIT Baseline Vibration Isolation Control System," *Proceedings of AIAA guidance,navigation and control conference*, AIAA 2002-5019, Denver, Co, August 2002.

[9] Whorton, M., "Robust Control for the g-LIMIT Microgravity Vibration Isolation System," *AIAA Journal of Spacecraft and Rockets*, Vol. 42, No. 1, 2005.

[10] Shkolnikov, I., Shtessel, Y., Whorton, M. S., and Jackson, M., "Microgravity Isolation Control System Design via High-Order Sliding Mode Control," *Proceedings of the American Control Conference*, Chicago, IL, June 2000, pp. 2072–2076.

[11] Hovakimyan, N., Yang, B.-J., and Calise, A., "An Adaptive Output Feedback Control Methodology for Non-Minimum Phase Systems," *Proceedings of Conference on Decision and Control*, Las Vegas, NV, 2002, pp. 949–954.

[12] Yang, B.-J., Hovakimyan, N., Calise, A., and Craig, J., "Experimental Validation of an Augmenting Approach to Adaptive Control of Uncertain Nonlinear Systems," *Proceedings of AIAA guidance,navigation and control conference*, AIAA-2003-5715, Austin, TX, 2003.

[13] Hornik, N., Stinchcombe, M., and White, H., "Multilayer feedforward networks are universal approximators," *Neural Networks*, Vol. 2, 1989, pp. 359–366.

[14] Ge, S., Lee, T., and Harris, C., *Adaptive Neural Network Control of Robotic Manipulators*, World Scientific, 1998.

[15] Lewis, F., Jagannathan, S., and Yeşildirek, A., *Neural Network Control of Robot Manipulators and Nonlinear Systems*, Taylor & Francis, 1999.

[16] Spooner, J. T., Maggiore, M., Ordóñez, R., and Passino, K. M., *Stable Adaptive Control and Estimation for Nonlinear Systems- Neural and Fuzzy Approximator Techniques*, John Wiley & Sons, New York, NY, 2002.

[17] Hovakimyan, N., Nardi, F., Calise, A., and Lee, H., "Adaptive Output Feedback Control of a Class of Nonlinear Systems Using Neural Networks," *International Journal of Control*, Vol. 74, No. 12, 2001, pp. 1161–1169.

[18] Lavretsky, E., Hovakimyan, N., and Calise, A., "Upper Bounds for Approximation of Continuous-Time Dynamics Using Delayed Outputs and Feedforward Neural Networks," *IEEE Transactions on Automatic Control*, Vol. 48, No. 9, 2003, pp. 1606–1610.

[19] Kim, N., Calise, A. J., Hovakimyan, N., Prasad, J., and Corban, J. E., "Adaptive Output Feedback for High-Bandwidth Flight Control," *AIAA Journal of Guidance, Control & Dynamics*, Vol. 25, No. 6, 2002, pp. 993–1002.

[20] Calise, A., Yang, B.-J., and Craig, J., "An Augmenting Adaptive Approach to Control of Flexible Systems," *AIAA Journal of Guidance, Control & Dynamics*, Vol. 27, No. 3, 2004, pp. 387–396.

[21] Yang, B.-J., Calise, A., and Craig, J., "Adaptive Output Feedback Control of a Flexible Base Manipulator," *Proceedings of AIAA guidance,navigation and control conference*, AIAA-2004-5322, Providence, RI, August 2004.

[22] Calise, A., Hovakimyan, N., and Idan, M., "Adaptive Output Feedback Control of Nonlinear Systems using Neural Networks," *Automatica*, Vol. 37, No. 8, 2001, pp. 1201–1211.

[23] Hovakimyan, N., Nardi, F., Kim, N., and Calise, A., "Adaptive Output Feedback Control of Uncertain Systems using Single Hidden Layer Neural Networks," *IEEE Transactions on Neural Networks*, Vol. 13, No. 6, 2002.

[24] Balas, M. J., "Direct Velocity Feedback Control of Large Space Structures," *AIAA Journal of Guidance, Control & Dynamics*, Vol. 2, No. 3, May-June 1979, pp. 252–253.

[25] Isidori, A., *Nonlinear Control Systems*, Springer-Verlag, Berlin;New York, 3rd ed., 1995.

[26] Hovakimyan, N., Yang, B.-J., and Calise, A. J., "Adaptive Output Feedback Control Methodology Applicable to Non-Minimum Phase Nonlinear Systems," *Automatica*, Vol. 42, No. 4, April 2006, pp. 513–522.

[27] Isidori, A., *Nonlinear Control Systems II*, Springer-Verlag, London, 1999.

[28] Hovakimyan, N., Lavretsky, E., Yang, B.-J., and Calise, A., "Coordinated Decentralized Adaptive Output Feedback for Control of Interconnected Systems," *IEEE Transactions on Neural Networks*, Vol. 16, No. 1, 2005, pp. 185–194.